Journal of Materials Chemistry A

REVIEW

Check for updates

Synchrotron-radiation spectroscopic identification towards diverse local environments of single-atom catalysts

Sicong Qiao,† Qun He, †† Pengjun Zhang, Yuzhu Zhou, Shuangming Chen, ID Li Song ID * and Shiqiang Wei ID *

Single-atom catalysts (SACs) that can achieve maximum atom utilization and provide well-defined active sites in energy conversion reactions have attracted much attention in the past decade. In general, the local structures of active sites in SACs largely determine their catalytic activity and selectivity. Therefore, identifying the local environments of active sites in specific SACs is essential to understand their catalytic functions in various reactions. Recent studies have demonstrated that synchrotron-radiation spectroscopic characterization methods possess unparalleled capacity in the identification of local environments of SACs due to their wide energy regulation window and high resolution. In this review, we aim to discuss the practical applications of some *ex/in situ* synchrotron-radiation spectroscopic techniques in recently reported advanced SACs. The experimental analyses from various techniques, such as X-ray absorption spectroscopy (XAS), photoemission spectroscopy (PES) and Fourier-transform infrared spectroscopy (FTIR), are highlighted. The built structure–activity relationships towards identified active sites are also discussed. Finally, a summary of spectral imputs and related significance is made and the research perspectives are suggested.

1. Introduction

With the rapid development of world-wide industrialization and frequent human activity, the global consumption of fossil fuels is ever-increasing; inevitably, the shortage of natural resources and environmental problems, such as ocean acidification,

National Synchrotron Radiation Laboratory, CAS Center for Excellence in Nanoscience, University of Science and Technology of China, Hefei, Anhui 230029, China. E-mail: song2012@ustc.edu.cn; sqwei@ustc.edu.cn

† These authors contributed equally to this work.

greenhouse effect, *etc.*, have happened.[1,2] To mitigate these problems, many scientists call to increase the proportions of clean and sustainable solar, hydrogen, wind and other energy sources in modern energy supply systems.[3–5] However, these energy sources are intermittent, largely hampering their practical applications. To address this issue, many researchers have proposed to develop efficient energy conversion and storage devices based on electrochemistry, photochemistry or thermochemistry in the past decades.[6,7] Generally, the design and operation of these energy devices involve some typical catalytic reactions, *i.e.*, hydrogen evolution reaction (HER), hydrogen

This journal is © The Royal Society of Chemistry 2022

J. Mater. Chem. A, 2022, **10**, 5771–5791 | 5771

oxidation reaction (HOR), oxygen evolution reaction (OER), oxygen reduction reaction (ORR), carbon dioxide reduction reaction (CO_2RR), Fischer–Tropsch synthesis (FTS), *etc.*[8–13] These reactions with complicated and sluggish reaction pathways are hard to achieve superior performances to meet the demands of energy devices. For example, the four concerted proton–electron transfer process involved anodic OER just possesses low capacity for oxygen formation, thereby limiting the rate of cathodic hydrogen production in water splitting.[14,15] In addition, FTS for industrial coal-to-liquid and gas-to-liquid processes has huge challenges in product selectivity control.[13] Therefore, exploiting high-activity catalysts is essential to promote the applications of energy devices.[16–18]

Traditional heterogeneous solid catalysts feature metal nanoparticles (NPs) and clusters that are composed of distinct amounts of metal atoms, and only a small fraction of sites located at surface, edge, step and corner are exposed to the reactants for catalysis.[19,20] Therefore, the atomic efficiency of traditional solid catalysts is very low, causing huge waste of metals, especially some noble metals.[21] Meanwhile, traditional catalysts endow the mechanism study with great challenges due to the presence of complex sites in them. Hence, the atomization strategy to decrease the size of metal particles/clusters into single atom to build single-atom catalysts (SACs) should be a promising way to inherit the advantages from both homogeneous and heterogeneous catalysts, such as maximum atomic utilization, high activity and stability.[22–24] However, significantly increased surface free energy with downsizing particles leads to the severe segregation of metal atoms in fabrication and employment processes, which is the culprit of low loading and instability of SACs.[25,26] Regarding this issue, some researchers found that appropriate supports with diverse anchoring and adsorption sites can prevent the sintering of single atoms (SAs) efficiently (Fig. 1).[27] It is also found that supports can work as the modifiers to influence the electronic configurations of foreign atoms through the strong metal-support interaction (SMSI).[28] Among different support materials, defect-rich nanocarbons, such as carbon nanotubes, graphene and carbon nitride, have been widely discussed.[29–31] Intrinsic edges and holes, doped heteroatoms and surface function groups in/on nanocarbons strengthen the binding of metal atoms *via* chemical coordination.[32–36] Metal compounds including oxides, nitrides, sulfides, phosphides, hydroxides, *etc.*, are also promising supports for SACs.[37] The existing cation/anion vacancies and large lattice voids in them can stabilize foreign atoms effectively, rendering obtained catalysts with excellent performances in various reactions.[38,39] In addition, atomic replacement between host and foreign atoms can also achieve the incorporation of single atoms.[40] Analogously, introducing isolated atoms into traditional metallic catalysts is also feasible, and these catalysts are generally known as single atom alloys (SAAs).[41,42] SACs can also be derived from some porous materials including metal–organic frameworks (MOFs), covalent organic frameworks (COFs) and zeolitic imidazole frameworks (ZIFs).[43–45] The ordered atomic arrangements, large atomic distance, and rich coordination atoms in them ensure the monodispersion of metal atoms after thermal pyrolysis.[46–48]

Based on the above analyses, it is easily found that the flexible collocation between active metal atoms and supports results in the formation of SACs with diverse local environments. Different environments endow SACs with distinct properties, thus meeting a series of reactions.[49] It is proved that the local cooperation between atomic Sn sites and adjacent oxygen vacancies in CuO contributes to higher CO_2-to-methanol selectivity and activity owing to more stable configuration of adsorbed COOH.[50] Moreover, some works demonstrated that the adjustment of ligand elementary species and coordination number can not only regulate the properties of metal sites, but also change the active centers. Tang *et al.* clarified that elements (N or O) in the first and second coordination spheres have a deep impact on the performance of Co SACs in acidic ORR.[51] Changing Co–N tetra-coordination of prevalent CoN_4 moieties to both Co–O and Co–N di-coordination for CoNOC moieties, the acidic ORR selectivity is tailored from $4e^-$ to $2e^-$ pathway

Li Song received his PhD in 2006 from Institute of Physics, Chinese Academy of Sciences (advisor Prof. SiShen Xie). He was promoted to professor at University of Science and Technology of China in 2012. He has published about 300 co-authored papers and been cited over 25 000 times in total with H-index 82. His research is focusing on the combination of synchrotron radiation multi-techniques (XAS, SR-XRD, SR-PES and SR-FTIR) via setting up online test platforms, together with the development of data processing method, and applying for the key scientific issues in dynamic reactions and related energy devices.

Shiqiang Wei received his PhD in 1992 from University of Science and Technology of China (advisors Prof. Qiwu Wang and Prof. Chengzong Yang). He was promoted to professor at University of Science and Technology of China in 1999. He was awarded the National Funds for Distinguished Young youths, and the Ministry of science and technology "973" project and National Key Basic Research Program of China. He has been engaged in establishment of X-ray absorption fine structure spectroscopy (XAFS) techniques with surface-sensitive, real-time and in situ measurement, and XAFS applications in energy conversion materials.
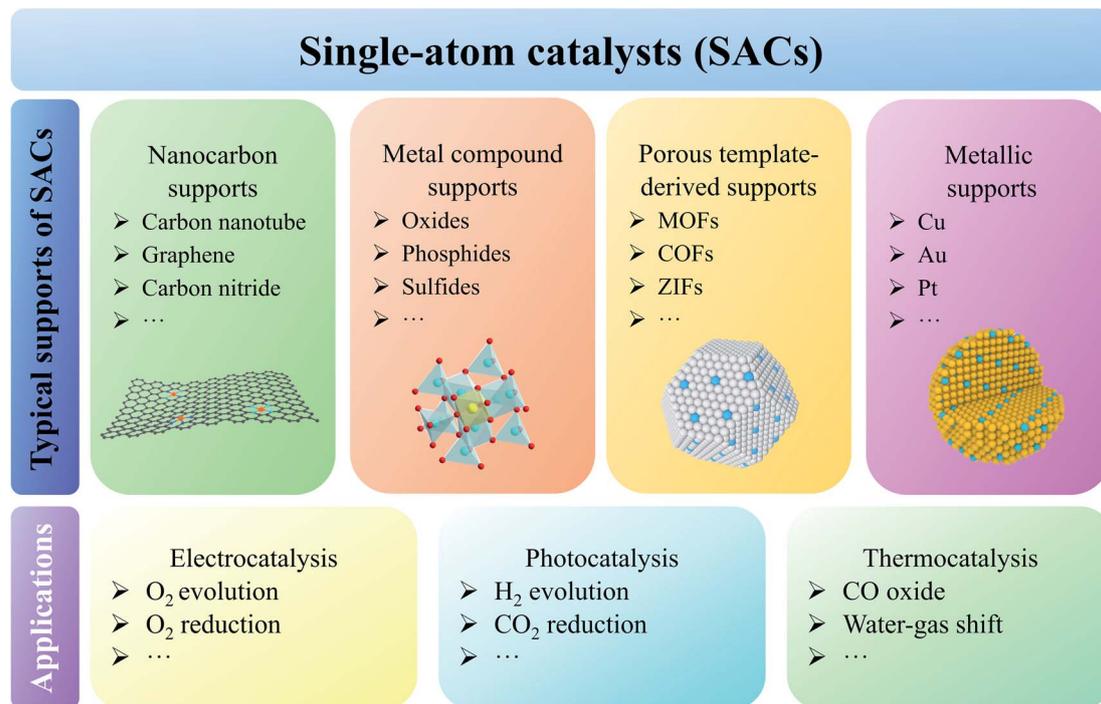
5772 | *J. Mater. Chem. A*, 2022, **10**, 5771–5791

This journal is © The Royal Society of Chemistry 2022

Single-atom catalysts (SACs)

Typical supports of SACs

Nanocarbon supports
➢ Carbon nanotube
➢ Graphene
➢ Carbon nitride
➢ …

Metal compound supports
➢ Oxides
➢ Phosphides
➢ Sulfides
➢ …

Porous template-derived supports
➢ MOFs
➢ COFs
➢ ZIFs
➢ …

Metallic supports
➢ Cu
➢ Au
➢ Pt
➢ …

Applications

Electrocatalysis
➢ O_2 evolution
➢ O_2 reduction
➢ …

Photocatalysis
➢ H_2 evolution
➢ CO_2 reduction
➢ …

Thermocatalysis
➢ CO oxide
➢ Water-gas shift
➢ …

Fig. 1 Comprehensive description of typical supports and applications of SACs.

while catalytic sites from isolated Co to C adjacent to the coordinated O. Li *et al.* reported a mixed catalyst containing both tetra-coordinate Zn–N_4 and unsaturated Zn–N_3 sites.[52] And these unsaturated atoms result in the lower oxidation state of Zn and more stable COOH* adsorption, contributing to the robust CO_2RR activity. On the other hand, high-loading SACs attract much attention and need to be explored to meet the demands of practical applications.[53–55] Benefiting from the strong chelation and self-assemble effect of amine-functionalized graphene quantum dots (GQDs-NH_2), the concentrations of isolated Ir and Ni sites can reach 41.6 wt% and 15.3 wt%, respectively.[56] Meanwhile, unveiling the unique coordinate configurations influenced by the increasing metal coverage is fundamental for tracking the activity origin and optimizing design strategies of SACs. For instance, Xiong *et al.* demonstrated achieving a remarkable Fe loading ratio value of 30 wt% in single-atomic-site (SAS) catalysts would decrease the coordinate number of Fe with appropriate ~2, which takes charge of the effective epoxidation of styrene.[57] These results elucidate that unveiling the atomic-level structures has great significance in cognizing the catalytic behaviors of SACs.

To unveil the local structures of SACs, traditional light source-based spectral characterization methods, such as X-ray photoelectron spectroscopy (XPS), ultraviolet photoelectron spectroscopy (UPS), Raman, Fourier-transform infrared spectroscopy (FTIR), *etc.*, are adopted in most works.[58] Although many valuable results have been obtained based on these methods, it is still desired to use higher resolution methods to uncover the unknown or uncertain.[59] In addition, traditional characterization methods in analyzing SACs face huge challenges. One challenge is that SACs generally have much less atomic concentrations than their nanoparticles and clusters. Another challenge is the smallest size disables some traditional structure characterization methods including X-ray diffraction (XRD), angle-resolved photoemission spectroscopy (ARPES), *etc.* As known, high-quality light source is one of the most important parts to determine the spectral signal-to-noise ratio (SNR) and resolution. In this regard, synchrotron-radiation light with high collimation, high resolution and continuously adjustable energy, performs huge advantages relative to traditional light sources in multiply conditions.[60] The coupled X-ray absorption spectroscopy (XAS), including X-ray adsorption near-edge structure (XANES) and extended X-ray absorption fine structure (EXAFS), can be obtained in one test to analyze both electronic and coordinate structures of SACs. This advantage has been proved by many reported SACs-related works.[61,62] Moreover, it is worth noting that XANES and EXAFS measurements can be applied under working conditions to provide reality-close information for the in-depth cognition of activity origins and catalytic mechanisms of SACs. Besides XANES and EXAFS, soft XAS is also efficient in the detection of chemical states, orbital hybridization and atom-specific local environments of SACs.[63–65]

It is also demonstrated that establishing traditional characterization methods based on synchrotron-radiation light can improve their data quality and reliability to a large extent. For instance, synchrotron radiation XPS, one of the most important surface-sensitive characterization methods, can obtain the surface information of catalysts with high energy resolution.[66] Moreover, synchrotron-radiation near-ambient pressure X-ray photoelectron spectroscopy (NAP-XPS) or ambient pressure XPS (AP-XPS) is available for monitoring superficial valence
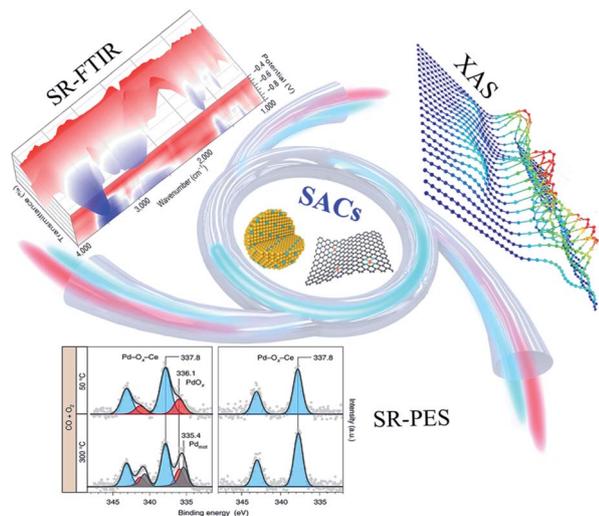
Fig. 2 Schematic illustration of characterization results obtained by typical synchrotron-radiation techniques for SACs. Reprinted with permission from ref. 73. Copyright 2021, Springer Nature. Reprinted with permission from ref. 138. Copyright 2021, Springer Nature.

states excluding the influence of ultrahigh vacuum (UHV).[67] Analogous to XPS, UPS is another surface-sensitive method which can probe the electronic levels and valence bands of materials near Fermi level (E_F).[68,69] The work functions detected by UPS represent the energetic barrier for donating electrons from the E_F of catalysts to the vacuum level or adsorbed molecules.[70] Generally, synchrotron-radiation XPS and UPS are collectively denoted as synchrotron radiation photoemission spectroscopy (SRPES) because of their identical principles with photoelectric effect.[71,72] In addition, *in situ/operando* synchrotron-radiation Fourier-transform infrared spectroscopy (SR-FTIR) is performed to certify the phase transition and identify the active intermediates.[73] Experimental reports have demonstrated that SR-FTIR can show exponential signal intensification with respect to traditional FTIR.[74] In conclusion, it is certain that synchrotron-radiation spectral methods are powerful in the identification of local environments of SACs. Hence in this review, we aim to summarize the advancements of multifarious synchrotron-radiation methods in parsing the local environments of SACs. These methods include XAS, SRPES and SR-FTIR (Fig. 2). The usage of *in situ/operando* synchrotron-radiation methods is expected to track the dynamic evolution of catalytically active sites at the beginning, proceeding and ending of reactions, understand the structure–property relationships, and provide the guideline for SACs designs. Finally, the capabilities and limitations of these methods are discussed for the demands of further development.

2. Synchrotron-radiation spectroscopies towards SACs

2.1 XAS

XAS is a synchrotron-radiation element-specific technique based on motivating electrons from the core to unoccupied

energy levels by X-ray, thus offering help for unveiling electronic and coordinate structures of catalysts.[75] When the X-ray passes through materials, the attenuated intensity is quantified by the absorption coefficient according to Beer's law.[76] The relation between absorption coefficient and incident X-ray energy is influenced by elementary chemical states and local environments, which can be divided into pre-edge, near-edge and extended-edge regions.[77] Pre-edge and near-edge regions are sensitive to oxidation states and electronic levels of detected elements, hence together referred to XANES.[78,79] With further increasing X-ray energy, electrons will be excited to continuum states in vacuum.[80] Ejected and back-scattered photoelectrons surrounding the absorbing atom lead to oscillation reflecting the coordination number and bond length in extended-edge region, which is denoted as EXAFS.[81,82] Wavelet transform EXAFS (WT-EXAFS) spectra, which has high resolution for both k and R spaces, provide more intuitive comparison in bond length to identify distinct coordinated configurations.[83,84] And through the least-squares fitting of Fourier transform EXAFS (FT-EXAFS), accurate values about coordinate number and bond length can be obtained.[85,86] Besides, soft XAS has unique advantages in investigating orbital hybridization between metal and light ligand elements by employing soft X-ray as the excited light source.[87]

Different from techniques focusing on superficial chemical environments like XPS, XAS implies total statistical results of catalyst bulks owing to superior penetration depth of X-ray, which makes visualizing *operando* and *in situ* variation of serving SACs possible (Fig. 3a and b).[88,89] Tracking the evolution of local environments including optimization of chemical states and bonding forms has attracted broad attention by *in situ* XAS under applied outfields. In this part, we are going to present more detailed discussions on identifying SACs with diverse local environments by XAS.

2.1.1 XANES. XANES can be used to evaluate elementary electronic structures directly and charge transfer indirectly, both of which are deeply connected with local environments of SAs.[90] Typically, the electronic transition peaks of metals in pre-edge region can provide fingerprint identification of coordinate information. For instance, He *et al.* synthesized a dual-site SAC (denoted as CoNi-NC) for electrochemical conversion of CO_2 to syngas.[91] Obtained from Co and Ni K-edge XANES profiles, the valence states of Co and Ni are between 0 and +2, excluding the existence of metallic Co and Ni (Fig. 3c and d). It is worth noting that weak signals in pre-edge region are corresponding to the 1s → 4p$_z$ transition of Co and Ni, which are fingerprint descriptors for square-planar M-N_4 moieties. Meanwhile, the reduced intensities compared to Co- and Ni-phthalocyanine suggest the distorted D_{4h} symmetry in CoNi-NC. Then coupling XPS and EXAFS spectra, the single-atom configuration with dominant tetra-pyridinic-N coordination is confirmed. The Co–N_4 and Ni–N_4 act as HER and CO_2RR sites respectively, which opens up the possibility of efficient production of syngas (Fig. 3e). Moreover, the electronic interaction regulated by metal compound supports through metal-nonmetal-metal bonds can be investigated by XANES. Shan *et al.* paid attention to short-range ordered Ir SAs integrated into cobalt oxide spinel (marked as

5774 | *J. Mater. Chem. A*, 2022, **10**, 5771–5791

This journal is © The Royal Society of Chemistry 2022

$Ir_{0.06}Co_{2.94}O_4$) synthesized by ion exchange–pyrolysis procedure (Fig. 4a).[92] XANES spectra show that Ir in $Ir_{0.06}Co_{2.94}O_4$ has a high valence state of about 4+, which acts as superior acidic OER sites (Fig. 4b and c). An increasing oxidation state of Co induced by electronic transfer after Ir substituting is proved through Co K-edge XANES (Fig. 4d).

In situ and *operando* XANES methods play a vital role in connecting local electronic environments of the target elements with reactivity and stability of SACs to conduct mechanism analysis.[93] In the above-mentioned Shan's work, *in situ* Co K-edge XANES spectra were recorded to observe Co oxidation states under OER condition.[92] Similar shape and intensities of white line suggest no obvious phase transformation under different applied potentials (Fig. 4e), in accordance with the results of *in situ* Raman spectra. These conclusions confirm Ir species can restrain the oxidation from Co_3O_4 to high-valence and easy-leaching $CoO_x(OH)_y$, which renders slighter dissolution of surface Co species than Co_3O_4 support and the long-term stability for over 200 h (Fig. 4f).[94] Otherwise, the reactive evolution of local environments, such as reversible clustering of SAs, has a strong impact on catalytic performances, which can be specialized by the linear combination fitting (LCF) of *in situ* and *operando* XANES spectra. Maurer *et al.* fabricated Pt single-site catalyst (Pt-SS) through the redispersion of a traditional Pt/CeO₂ catalyst in the hydrothermal oxidizing treatment.[95] Using original Pt-SS and Pt nanoparticles (Pt-NP) as references for transiently recorded *operando* XANES spectra, obvious

reduction in Pt-SS is observed when CO conversion set in, while absence in Pt-NP (Fig. 5a). Complementary to *in situ* infrared (IR) spectroscopy and DFT calculations, *operando* and *in situ* high-energy-resolution fluorescence detected XANES (HERFD-XANES) spectra were performed to track the formation, fate and consequence of Pt-SS. A dramatic decrease in intensity up to 150 °C arises followed by a shift of the white line towards lower adsorption energy (Fig. 5b), which certifies the valence of Pt changes accompanied by CO adsorption. To interpret the intermediate structural states, LCF was performed for *operando* spectra using the references obtained from the multivariate curve resolution alternating least squares algorithm (MCR-ALS) of *in situ* spectra.[96,97] Four reference compounds containing Pt^{4+}, Pt^{2+}, more reduced $Pt^{\delta+}$–CO and Pt cluster-like $Pt_x^{\delta+}$–CO are proposed and quantificationally assigned to HERFD-XANES experimental spectra verified by *ab initio* calculations using FDMNES code (Fig. 5d–f).[98,99] Ultimately, the relationship between fractions of references and applied temperatures indicates that formed tiny $Pt_x^{\delta+}$ entities from the breaking of Pt–O–Ce bonds work as real active sites for CO conversion (Fig. 5c).

Thus, positive oxide states of metal atoms confirmed by XANES are indirect proofs to exclude the presence of metallic phase.[100] The contrast of elementary electronic structures before and after introducing SAs is proceeded to specialize electron transfer and SMSI by *ex situ* XANES spectra.[101,102] On the other hand, visualizing the dynamic changes of oxidation states is crucial to investigating the evolution of single-atom
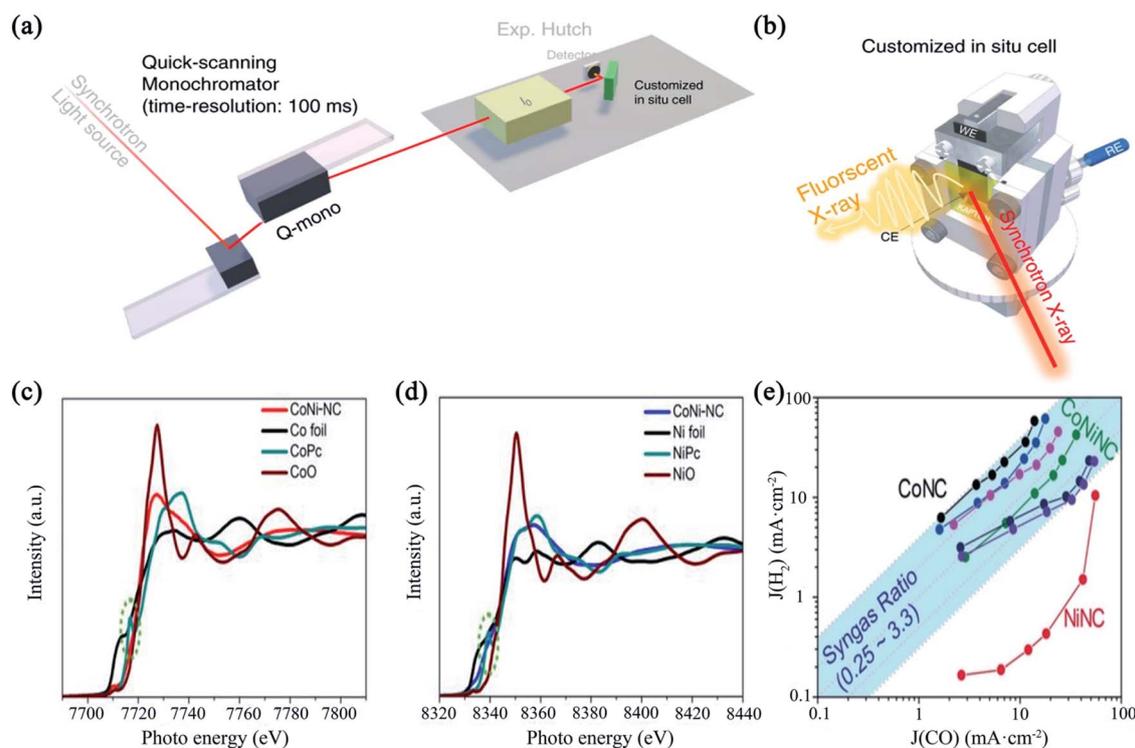

Fig. 3 (a) The schematic diagram of a kind of setup for *operando* time-resolved XAS experiments; (b) the cartoon representation of customized operando XAS cell. Reprinted with permission from ref. 88. Copyright 2020, Springer Nature. (c, d) Co and Ni K-edge spectra of CoNi-NC and references; (e) the corresponding current densities of CO and H₂. Reprinted with permission from ref. 91. Copyright 2020, WILEY-VCH Verlag GmbH & Co. KGaA, Weinheim.
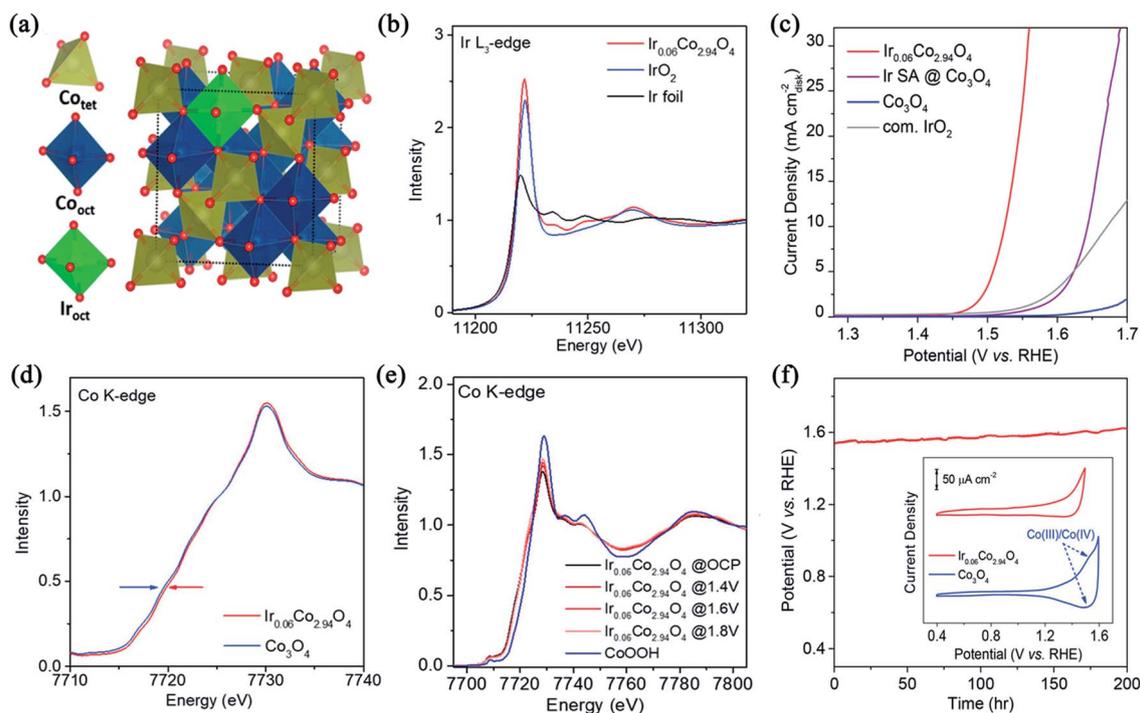
Fig. 4 (a) Structural model of Ir-substituted cobalt spinel oxide in a polyhedral representation; (b) Ir L_3-edge spectra of $Ir_{0.06}Co_{2.94}O_4$, IrO_2 and Ir foil; (c) polarization curves in O_2-saturated 0.1 M $HClO_4$; (d) Co K-edge spectrums of $Ir_{0.06}Co_{2.94}O_4$ and Co_3O_4 support; (e) *in situ* Co K-edge spectra under several potentials; (f) chronopotentiometric curve of $Ir_{0.06}Co_{2.94}O_4$ at 10 mA cm^{-2}, the insert is cyclic voltammetry (CV) tests. Reprinted with permission from ref. 92. Copyright 2021, American Chemical Society.

environments and impact of relevant adsorbed molecules under serving conditions, which can be achieved by *in situ* and *operando* XANES spectra cooperating with IR, Raman, theoretical calculation, *etc.*[103] In general, synchrotron-radiation XANES takes momentous effect in unveiling redox-involved reaction mechanisms.

2.1.2 EXAFS. EXAFS studies contribute to analyzing local coordinate configurations including bond length and ligancy of elements, thus giving detailed descriptions of structural models for SACs. It is reported that the catalyst with Ni SAs immobilized on N-doped hollow carbon spheres (Ni SACs/N–C) acts as an electrochemical sensor providing the real-time monitoring for cellular NO with a nanomolar detection limit (Fig. 6a).[104] Least-squares fitting of FT-EXAFS spectrum exhibits only one dominant Ni–N peak with tetra coordination (Fig. 6b), suggesting a highly dispersed Ni–N$_4$ architecture. Theoretically calculated spectrum employing the model of Ni–N$_4$ immobilized on graphene is most consistent with the experimental one (Fig. 6c), which further manifests the geometrical aspects of Ni SACs/N–C. Moreover, it is well known that the performances of SACs can be rationally optimized by tailoring the metal atoms,[105,106] adjacent coordinative dopants,[107,108] and metal loading.[109,110] Thus the impacts of unique coordinate structures and increasing metal loading on structure–property relation have been discussed extensively. Tang *et al.* prepared a new kind of Mo SAC (Mo$_1$/OSG-H) with the loading ratio reaching 13.47 wt% by MgO-templated pyrolysis combined with glucose-chelating and defect-trapping effects.[111] Owing to the heterogeneity

induced by such a high Mo loading amount, EXAFS fitting with both Mo–O$_3$S–C and mixture (Mo–O$_4$–C and MoS$_2$) models disables to give reasonable results. However, comparing to Na$_2$MoO$_4$ and MoS$_2$ references, the features of Mo–O and Mo–S bonds can be identified unambiguously from FT-EXAFS and WT-EXAFS, which suggests a mixed coordination of Mo–O and Mo–S moieties in isolated Mo atoms anchored on oxygen, sulfur co-doped graphene (Fig. 6d and e). Benefiting from this novel structure and impressive metal concentration, Mo$_1$/OSG-H exhibits the remarkable activity and selectivity over 95% towards 2e$^-$ ORR pathway (Fig. 6f). Besides classical coordination with heteroatoms like N, O, S, *etc.*, metal–metal bonds can also take effect in trapping and immobilizing isolated atoms. For instance, Liu *et al.* achieved the transformation from RuO$_2$ aggregates to Ru SAs (Ru$_1$/MAFO) arising from anti-Ostwald ripening promoted by a strong covalent metal–support interaction (CMSI).[112] EXAFS spectrum of Ru$_1$/MAFO-900 reveals Ru–O and Ru–Fe scattering contributions (Fig. 7a), and the absence of Ru–Ru and Ru–O–Ru unambiguously evidences high dispersion of Ru atoms. Then combining multiply characterization methods, it is proved that the presence of Ru–Fe indicates CMSI between Ru SAs and FeO$_x$ can trap and stabilize Ru atoms after high-temperature calcination at 900 °C, which also contributes to the excellent performances for N$_2$O decomposition (Fig. 7b and c).

In situ and *operando* EXAFS spectra also pave a way for observing the dynamic reconstruction of local structures and formation of real catalytic active sites of SACs, which helpfully
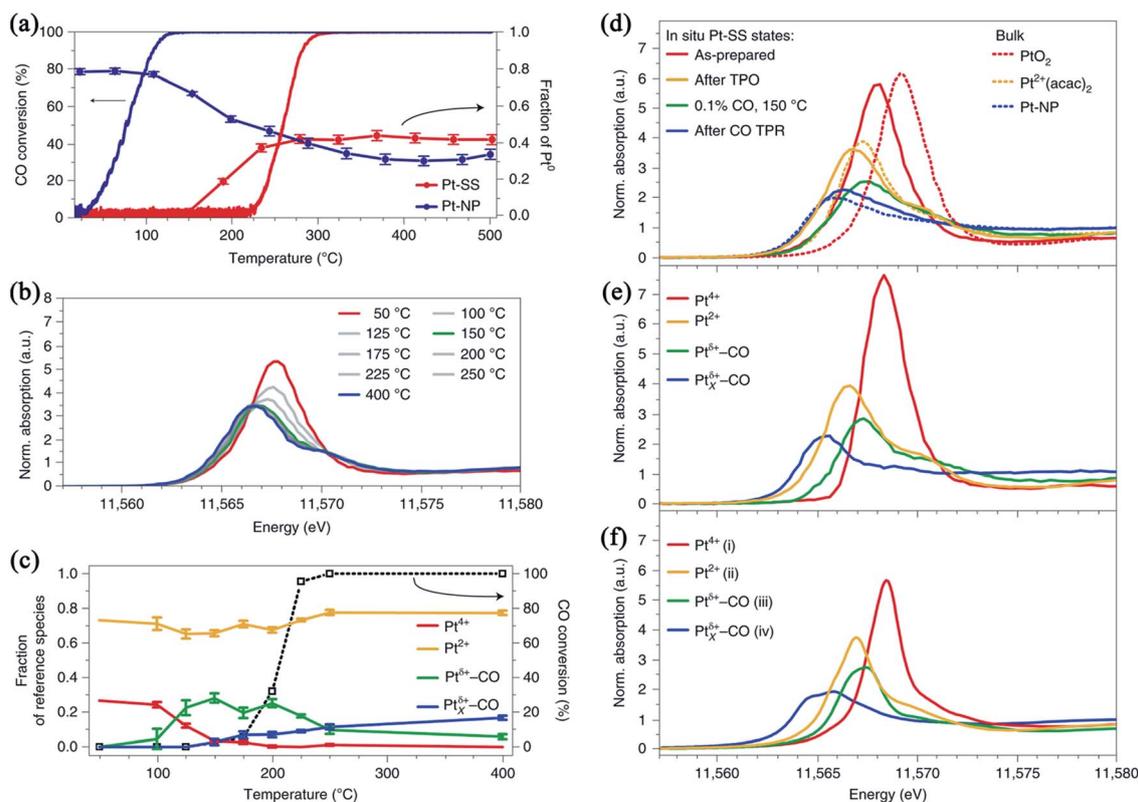
5776 | *J. Mater. Chem. A*, 2022, **10**, 5771–5791

This journal is © The Royal Society of Chemistry 2022

Fig. 5 (a) CO conversion and LCF results of transiently recorded spectra during heating with 5 K min^{-1} in 1000 ppm CO and 10% O$_2$ in He; (b) *operando* HERFD-XANES spectra of Pt-SS recorded at different temperatures in the gas mixture including 1000 ppm CO, 10% O$_2$ and He; (c) catalytic activity during the HERFD-XANES experiments and fraction of Pt species obtained by LCF using references proposed by MCR-ALS; (d) *in situ* experimental spectra under the treatment of temperature-programmed reduction (TPR) and temperature-programmed oxidation (TPO); (e) spectra of MCR-ALS-derived references; (f) FDMNES-calculated spectra. Reprinted with permission from ref. 95. Copyright 2020, Springer Nature.

operates mechanism analysis. Xu *et al.* synthesized a carbon-supported atomically dispersed Cu catalyst by amalgamated Cu–Li and subsequent leaching away Li.[113] *Ex situ* EXAFS spectra demonstrate single Cu is coordinated with four oxygen atoms and no Cu–Cu bond appears while the loading ratio is inferior to 0.4 wt% (Fig. 7e), agreeing well with the LCF of XANES. It's also found that Cu keeps atomically dispersed after a 16 h chronoamperometric run at −0.7 V for Cu/C-0.4. Then *operando* EXAFS spectra of Cu/C-0.4 were collected. Once the cell voltage was applied at −0.7 V, Cu first shell coordination switched from Cu–O to mainly Cu–Cu, indicating the formation of clustering Cu entities (marked as Cu$_n$, where n = 3 or 4) that act as catalytically active sites for CO$_2$RR (Fig. 7f and g). Meanwhile, the re-oxidation of Cu$_n$ clusters to Cu^{2+} SAs occurs in the CO$_2$-saturated electrolyte as soon as the voltage shuts down according to *ex situ* EXAFS. Incorporating DFT calculations, the CO$_2$-to-ethanol paths including a reversible transformation between Cu clusters and SAs was proposed in Fig. 7c. Moreover, some comparatively slighter changes in local environments are also associated with catalytic activities, such as shrinking or stretching of chemical bonds. Shang *et al.* designed a single-atom In$^{δ+}$–N$_4$ catalyst (In-SAs/NC) through wet-impregnation and pyrolytic processes, the structure of which is confirmed by *ex situ* quantitative EXAFS (Fig. 8a).[114] WT-EXAFS spectrum

shows strong signal for In–N instead of In–In (Fig. 8d). Then potential-dependent *in situ* XAFS was conducted to observe the change of In–N bonds (Fig. 8b). It is analyzed that In–N bond length becomes shorter at −0.65 V than without potential, taking charge for high catalytic activity and selectivity of CO$_2$RR (Fig. 8c).

Therefore, EXAFS analysis is a mighty method to estimate dispersion degrees and distinguish the local environments of object elements by quantitative fit, especially for SACs.[115] However, *ex situ* EXAFS isn't sensitive to some reversible or surrounding-involved processes. In this case, *in situ* and *operando* EXAFS spectra are essential for conducting studies of catalytic mechanisms because of convenience to tracking the changes of bond length and coordinate features of metal SAs, which is closely connected with the self-optimization of catalysts. Combining *in situ* or *operando* XANES and EXAFS, a detailed reaction mechanism can be postulated.[116]

2.1.3 Soft XAS. The feature of relatively lower energy makes soft XAS sensitive to investigating the bond types and orbital hybridization of light elements.[117] Especially for some classical SACs with nanocarbon supports, ligand elements like C, N, O, S play a vital role in catalytic reactivity.[118] Zhang *et al.* obtained a HP-FeN$_4$ catalyst with high-purity pyrrole-type FeN$_4$ sites synthesized by pyrolysis under NH$_3$ atmosphere.[119] Traditional

This journal is © The Royal Society of Chemistry 2022

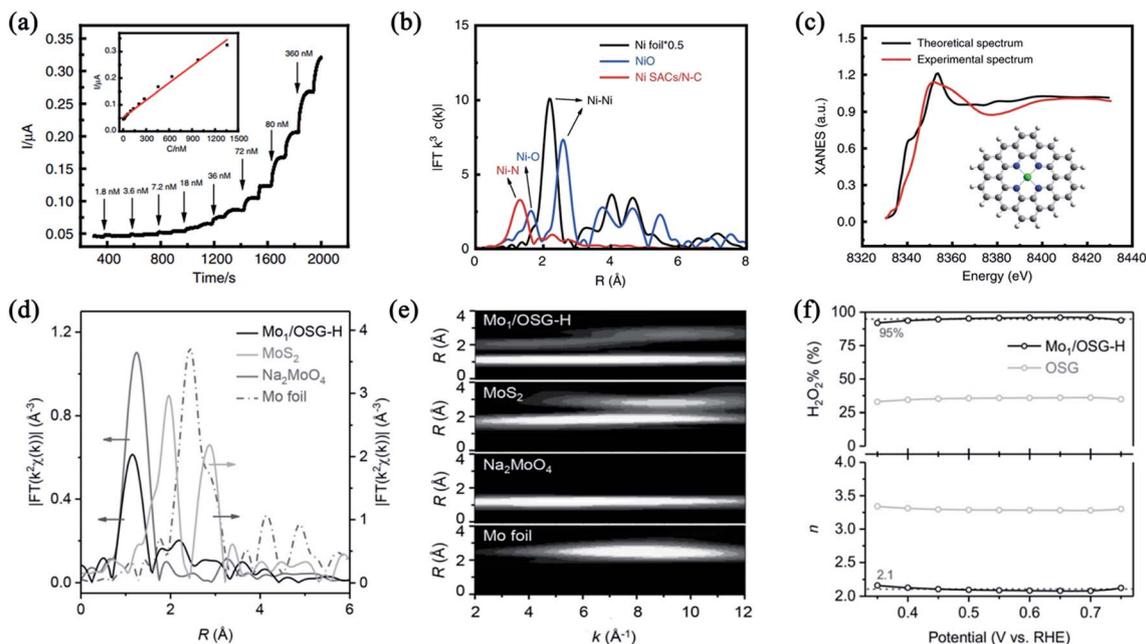*J. Mater. Chem. A*, 2022, **10**, 5771–5791 | **5777**

Fig. 6 (a) Amperometric response of the Ni SACs/N–C-based stretchable sensor to successive addition of NO at +0.80 V, the inset is calibration curve; (b) Ni K-edge FT-EXAFS spectra of Ni SACs/N–C, NiO and Ni foil; (c) experimental and calculated spectrums, inset is proposed Ni–N$_4$ architecture. Reprinted with permission from ref. 104. Copyright 2020, Springer Nature. (d, e) FT- and WT-EXAFS curves of the Mo K edge; (f) calculated electron transfer number (n) and H$_2$O$_2$ selectivity (H$_2$O$_2$%) of Mo$_1$/OSG-H. Reprinted with permission from ref. 111. Copyright 2020, WILEY-VCH Verlag GmbH & Co. KGaA, Weinheim.

FeN$_4$ sites were also fabricated analogically except under Ar atmosphere. Two typical features in C K-edge soft XAS of HP-FeN$_4$ and FeN$_4$ are assigned to the 1s core electrons of C into the $\pi_{C=C}$* and σ_{C-C}* respectively, which is similar to highly graphitized carbon (Fig. 9a left). Spontaneously, N K-edge soft XAS can also be divided into two regions containing 1s electrons into the π* and σ* (Fig. 9a right). The transition from 1s to π* presents obvious resonances ascribed to C–N–C portion of pyridinic N (peak a) and pyrrolic/graphitic type N-groups (peak b). To distinguish the coordinated N entities, peak a and b are fitted and the results confirm the existence of high-purity Fe–pyrrolic N sites in HP-FeN$_4$, which is entirely different from Fe–pyridinic N sites in FeN$_4$ (Fig. 9b and c). It means that neighboring N configuration around Fe changes from pyridinic to pyrrolic N with the assistance of NH$_3$, inducing preferable O$_2$ adsorption energy and superior activity for four-electron ORR (Fig. 9d). Besides aiming at ligand elements, soft XAS also contributes to analyzing species and distribution of transition elements through their L and M edges. It is reported that the Mn–O$_3$N$_1$ configuration anchored on porous carbon (Mn–O$_3$N$_1$/PC) was designed through a dissolution-and-carbonization method.[120] Mo L$_3$ soft XAS of Mn–O$_3$N$_1$/PC is similar to MnO reference in both total electron yield (TEY) and partial fluorescence yield (PFY) modes (Fig. 9e). This suggests the oxidation state of +2 and uniform dispersion of Mn, because TEY detects signals within 5–10 nm thickness of the surface while PFY within up to 100 nm thickness of the bulk.

It's worth noting that there are some researches concentrating on the influence of valence and spin states on catalytic

performance by *in situ* and *operando* soft XAS spectra. For example, Zhou *et al.* tracked the voltage- and time-proportional valence state transition of Co accompanied by spontaneous delithiation in Li$_2$Co$_2$O$_4$ under OER conditions by *operando* O K-edge soft XAS and ICP-OES.[121] Zheng *et al.* confirmed the formation of high-valence Ni^{4+} under low overpotential conditions during pH-neutral OER using *in situ* Ni L-edge soft XAS spectra.[122] However, the studies about *in situ* and *operando* soft XAS investigating on SACs are still lacking to the best of our knowledge, especially for light ligand elements. One possible reason is that soft XAS can only reflect the collective effect of C, N, O, *etc.*, while only a small portion of them are coordinated with center atoms, which makes the vibration too weak to detect.[123]

In summary, XAS spectra have powerful ability in discussing local characters including oxidation states, bonding forms and orbital hybridization. For SACs, the cationic feature and absence of metal–metal bonds deduced by XANES and EXAFS respectively are essential to confirm atomic dispersion. The puzzle about the metal–ligand interaction can be answered partially by soft XAS. Meanwhile, tracking outfield- and time-dependent vibration of SACs becomes possible owing to the development of *in situ* and *operando* XAS spectra. The identification towards local environments of catalysts is not restricted to the initial and final states any more, thereby contributing to understanding the evolution of active sites and conducting mechanism studies. However, some specific challenges still need to be overcome to get much more novel phenomena. For example, the sensitivity and detection limit should be optimized for the sake of receiving subtle responses, such as the
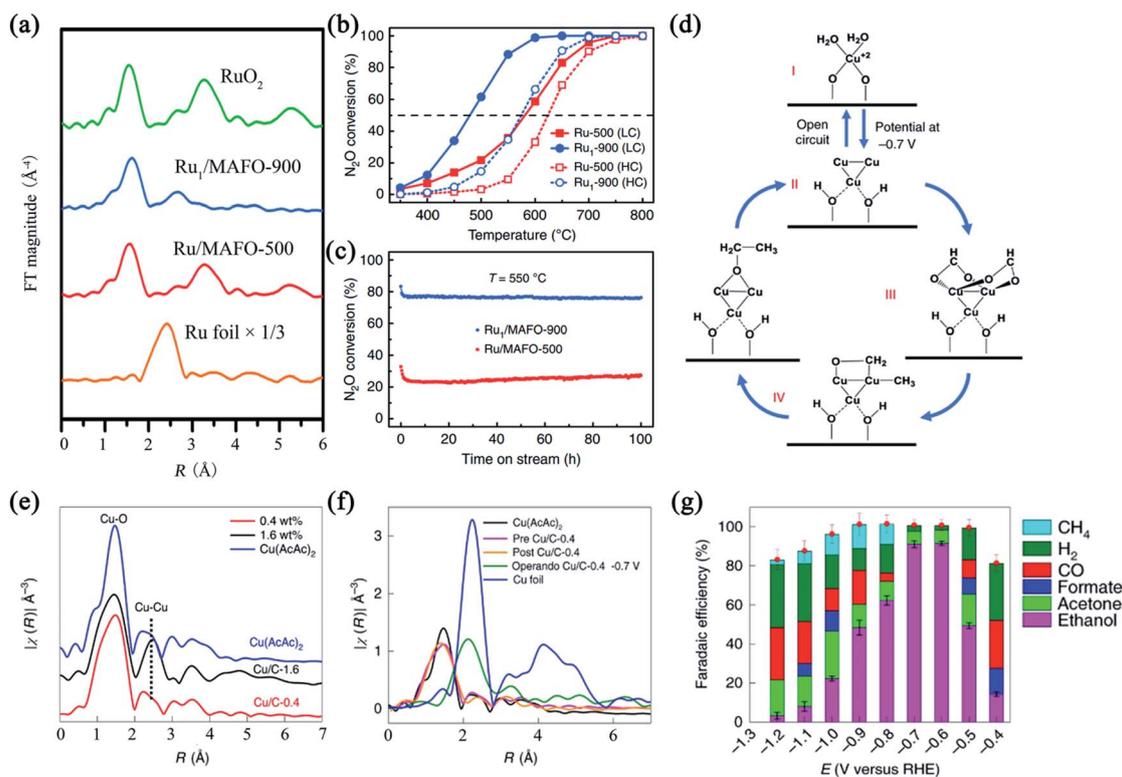
5778 | *J. Mater. Chem. A*, 2022, **10**, 5771–5791

This journal is © The Royal Society of Chemistry 2022

Fig. 7 (a) Ru K-edge spectra of Ru$_1$/MAFO, RuO$_2$ and Ru foil; (b) N$_2$O conversion at low (1000 ppm N$_2$O, solid symbol) and high (20 vol% N$_2$O, open symbol) concentrations; (c) N$_2$O conversion stability measurement in low concentration tested at 550 °C. Reprinted with permission from ref. 112. Copyright 2020, Springer Nature. (d) The hypothesized CO$_2$-to-ethanol reaction mechanism; (e) Cu K-edge spectra of Cu/C-0.4, Cu/C-1.6 and Cu foil; (f) *ex situ* and *operando* spectra, pre and post Cu/C-0.4 refer to the catalyst measured before and after CO$_2$RR respectively; (g) products' species and faradaic efficiency (FE) while employing Cu/C-0.4. Reprinted with permission from ref. 113. Copyright 2020, Springer Nature.
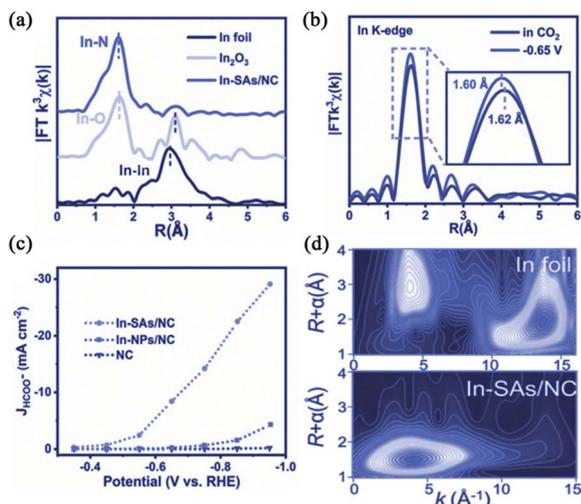

Fig. 8 (a) In K-edge spectra of In-SAs/NC, In$_2$O$_3$ and In foil; (b) *in situ* spectra of In-SAs/NC; (c) the current density of HCOO$^-$ in CO$_2$RR; (d) WT-EXAFS spectrums. Reprinted with permission from ref. 114. Copyright 2020, WILEY-VCH GmbH.

change of ligand elements and low-loading model SACs. The differential spectral method is another practical way to visualize these variations.[124,125]

2.2 SRPES

PES is a conventional, convenient and widely used method to evaluate the valence and species of target elements. Different from XAS detecting transmission light or fluorescence, PES receives signals from outgoing electrons that have shorter the mean free path due to inelastic collision.[126] Thus PES is sensitive to surface-involved systems, such as SAs immobilized on the surface of supports. Although most traditional XPS and UPS measurements are finished on lab-based devices, synchrotron-radiation light source can obtain more high-quality data at the same beamline due to the adjustable incident energy, high brightness, *etc.*[127]

Recently, quasi *in situ* synchrotron-radiation high-resolution XPS spectra referring to treating samples with distinct atmosphere and temperature in a reaction cell firstly, then transferring to the analysis chamber under UHV without exposure to air, is proposed for catalytic studies.[128–130] Although some valuable results have been obtained through quasi *in situ* XPS, it is worth noticing that this cannot avoid the influence of UHV on materials while testing. On the other hand, SACs-participating heterogeneous catalysis usually occurs on the solid–gas or solid–liquid interfaces. Authentic surface chemistry is a key descriptor for understanding catalytic performance.[131] Hence, synchrotron-radiation NAP-XPS attracts much attention in
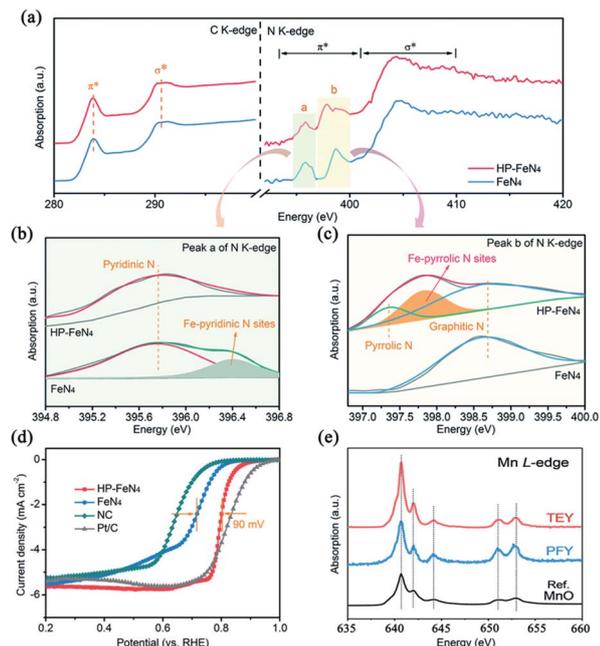
This journal is © The Royal Society of Chemistry 2022

J. Mater. Chem. A, 2022, **10**, 5771–5791 | 5779

Fig. 9 (a) C K-edge and N K-edge spectra of HP-FeN$_4$ and FeN$_4$; (b, c) deconvolution features of peak a (b) and b (c); (d) ORR polarization curves. Reproduced from ref. 119 with permission from the Royal Society of Chemistry. (e) Mn L-edge TEY and PFY spectra of Mn−O$_3$N$_1$/PC and MnO. Reprinted with permission from ref. 120. Copyright 2021, American Chemical Society.

investigating gas-involved processes and achieving *in situ* and *operando* tests, which are indispensable to understand paths of specially requested reactions (Fig. 10a).[132,133] Herein, synchrotron-radiation NAP-XPS and UPS were summarized to highlight the value for applying to SACs. Other issues solved by SRPES such as describing longitudinal distribution of elements are also noteworthy.[134]

2.2.1 NAP-XPS. As mentioned above, NAP-XPS builds the relation between local environments of SACs and interfaces surrounded by reactants. Liu *et al.* linked Ni^{2+} compound to carbon nanotubes (Ni-CNT-CC) as a well-defined single-atom Ni–N$_4$ model catalyst for efficient CO$_2$RR (Fig. 10b and c).[135] Almost the same intensity and shape in Ni 2p, O 1s, N 1s and C 1s NAP-XPS before and after exposing to 1 mbar CO$_2$ elucidates that CO$_2$ did not chemically interact with Ni^{2+} sites of Ni-CNT-CC (Fig. 10d–g). Combining *operando* Ni K-edge XANES, *operando* Raman spectra and electrochemical kinetics studies, reversible formed Ni$^+$ is certified as catalytically active centers for CO$_2$ activation.

Moreover, NAP-XPS is naturally appropriate for *in situ* and *operando* thermocatalytic conditions owing to the convertible atmosphere and temperature, so that tracking the dynamic evolution of local environments of active center atoms induced by gas reactants.[136] And unveiling these changes of coordinate types usually contributes to identifying real catalytic active species. For example, Wu *et al.* put forward a frustrated Lewis pair (FLP) mechanism of Ru anchored on stable MgO (111) facet for reversible hydrogen spillover based on *operando* AP-XPS
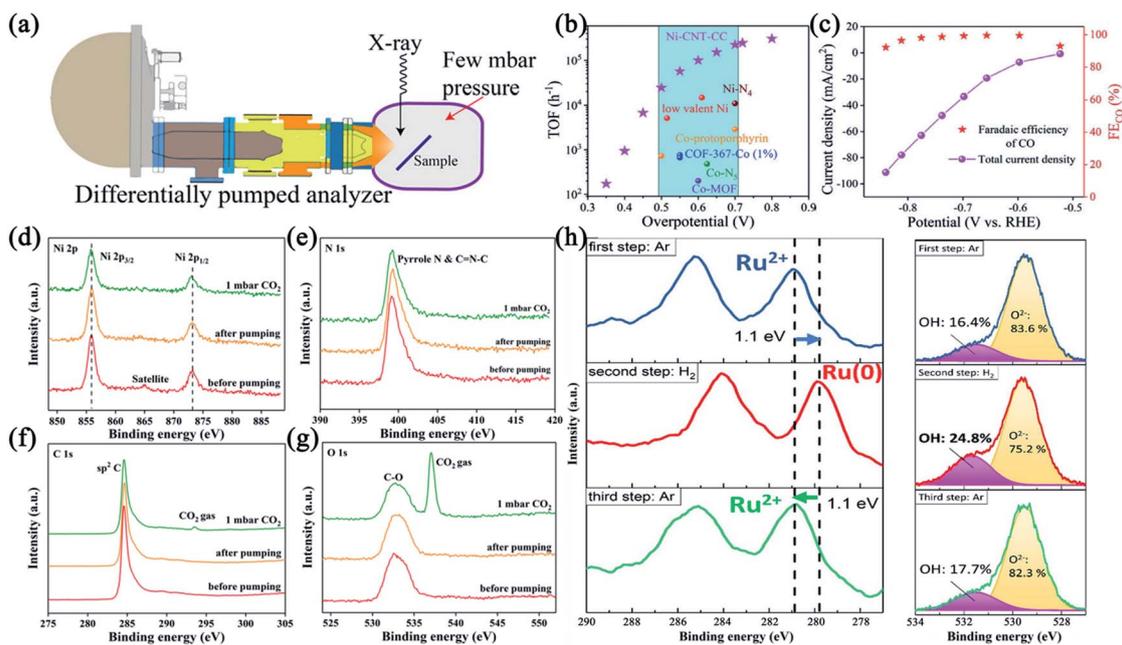

Fig. 10 (a) A schematic representation for NAP-XPS setup. Reprinted with permission from ref. 133. Copyright 2018, WILEY-VCH Verlag GmbH & Co. KGaA, Weinheim. (b) The TOF of Ni-CNT-CC compared with those of other state-of-the-art CO$_2$-to-CO reduction catalysts; (c) CO FE (symbol) and total current density (line + symbol); (d–g) high-resolution Ni 2p (d), N 1s (e), C 1s (f) and O 1s (g) spectra of Ni-CNT-CC before and after exposing to 1 mbar CO$_2$. Reprinted with permission from ref. 135. Copyright 2020, WILEY-VCH Verlag GmbH & Co. KGaA, Weinheim. (h) *Operando* Ru 3d (left) and O 1s (right) spectra of Ru/MgO (1 1 1) at 350 °C under switching between 1 mbar Ar and 1 mbar H$_2$. Reprinted with permission from ref. 137. Copyright 2021, American Chemical Society.

5780 | *J. Mater. Chem. A*, 2022, **10**, 5771–5791

This journal is © The Royal Society of Chemistry 2022

combining *in situ* diffuse reflectance infrared Fourier transform spectroscopy (DRIFTS) and *in situ* XANES spectra.[137] According to Ru 3d and O 1s XPS, after removing RuO_2 under H_2, Ru valence is +2 under Ar (Fig. 10h). Then switching to H_2 atmosphere, Ru is reduced to Ru(0) accompanied by a significant increase of OH in O 1s spectrum. The increase can be totally counteracted once the flowing gas is switched to Ar again, suggesting a reversible H_2 storage-release process. Under the circumstances, it is envisaged that half the reversible process is that Ru^{2+} acting as a Lewis acid leads to the cleavage of H_2 and formation of Ru–H hydride that is converted to a proton progressively along with the reduction of Ru, while O^{2-} near Ru sites as a Lewis base receives migrant proton to form OH^-. Muravev *et al.* compared the interface dynamics of two single-atom Pd/CeO_2 catalysts fabricated by conventional impregnation marked as 1PdRods and one-step flame spray pyrolysis (FSP) as 1PdFSP respectively for low-temperature CO oxidation.[138] *In situ* NAP-XPS demonstrates the appearance of small PdO_x clusters at 336.1 eV and even metallic Pd at 335.4 eV in 1PdRods while absence in 1PdFSP under 2 mbar pressure conditions including CO and O_2, showing the structural stability owing to stronger metal-support interactions (MSIs) by FSP (Fig. 11a and b). As a contrast, 5PdFSP and 5PdRods with higher Pd surface density are obtained to exclude the effect of Pd loading. Lower emerging temperature and content of metallic Pd in 5PdFSP are accord with mentioned conclusions, corroborated by *in situ* DRIFTS simultaneously. To understand MSIs and reducibility of the $Pd–CeO_2$ interfaces, *in situ*

synchrotron-radiation resonant photoelectron spectroscopy (RPES), with low excitation energies allowing visualizing elementary electronic states in the outermost layers at a depth less than $\sim$10 Å, was performed to track the variation of Ce^{3+} concentration by analyzing the Ce 4d–4f transition.[139,140] As shown in Fig. 11c and d, slightly higher Ce^{3+} ratio in 1PdFSP than 1PdRods and the bare FSP support suggests higher concentration of oxygen vacancies and surface reducibility induced by Pd doping. The high oxygen mobility at the $Pd–CeO_2$ interface supplies sufficient oxygen to stable cationic Pd.

In a word, *ex/in situ* and *operando* NAP-XPS for SACs are promising in conducting analysis of components with diverse local environments and mechanism studies of gas-involved interfacial processes. Meanwhile, NAP-XPS has developed a lot in gas pressure region and equipment design. Laboratory-based NAP-XPS systems have been used.[141] However, it should be highlighted that entropy of the gas phase of even 0.1–1.0 Torr can give rise to massive reconstruction of some catalysts, the influence of which cannot be estimated.[142] To reveal authentic surface chemistry of atmospheric processes, measurements in higher pressure even near 1 atm have to be exploited. On the other hand, current NAP-XPS characterizations mainly focus on pressure and temperature fields in gas phase catalysis. The applications of other outfields including electricity, magnetism and illumination need to be exploited for SACs-involved reactions.

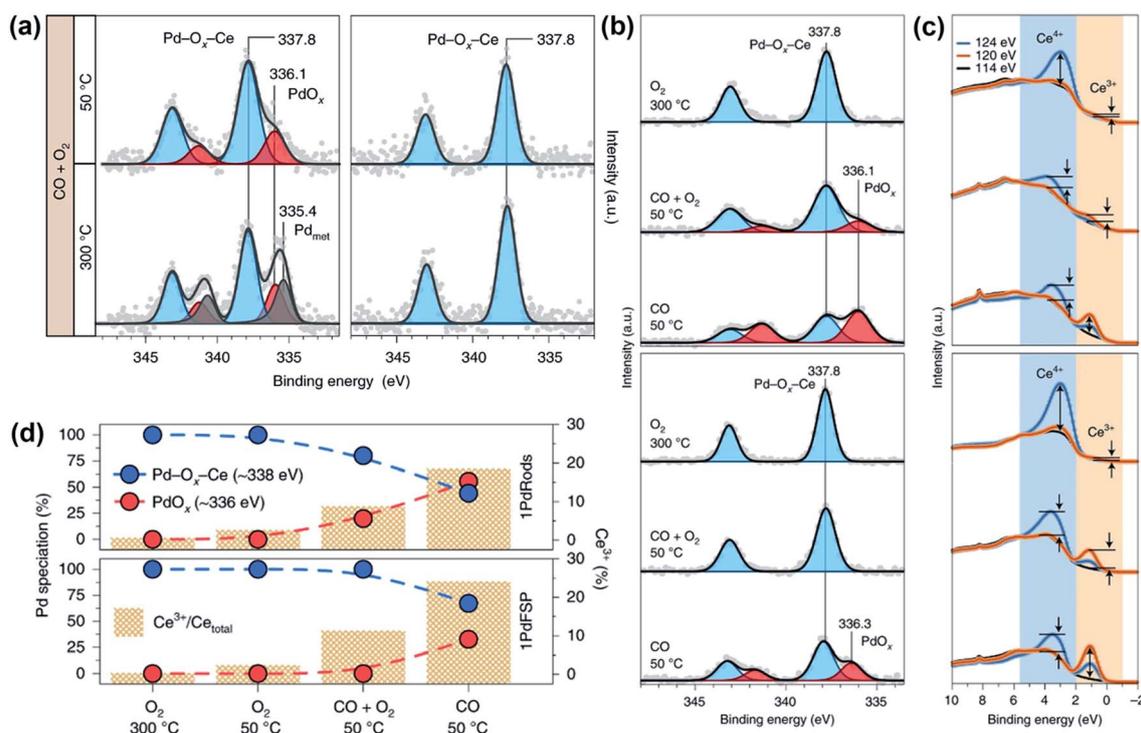**2.2.2 UPS.** UPS aims at evaluating electronic binding strength and flowing direction of catalysts. Although most UPS

Fig. 11 (a) *In situ* Pd 3d spectra of 1PdRods (left) and 1PdFSP (right) in 2 mbar mixed gas with CO : O_2 = 1 : 1 at applied temperature; (b, c) *in situ* XPS (b) and RPES (c) of 1PdRods (top) and 1PdFSP (bottom) in 0.1 mbar reactants; (d) Pd and Ce oxidation state derived from XPS and RPES data. Reprinted with permission from ref. 138. Copyright 2021, Springer Nature.

This journal is © The Royal Society of Chemistry 2022

J. Mater. Chem. A, 2022, **10**, 5771–5791 | **5781**

experiments apply ultraviolet light source generated by the de-excitation of excited atoms or ions (mostly helium I and helium II), synchrotron radiation light with broad wave band also covers the ultraviolet energy region.[143,144] The work function (Φ), which represents the energy difference between Fermi and vacuum level, can be calculated according to the formula $\Phi = h\nu - (E_{cutoff} - E_F)$, while $h\nu$, E_{cutoff}, E_F refers to incident light energy, secondary electron cutoff energy and Fermi energy.[145] Gao *et al.* demonstrated Co SAs immobilized on the partially oxidized graphene nanosheets (Co$_1$–G) with [Ru(bpy)$_3$]Cl$_2$ as a visible-light absorber for photocatalytic CO$_2$ conversion.[146] According to UPS with the excitation photon energy of 168.5 eV, the work function of Co$_1$–G is 4.9 eV referenced to the E_F = 0 determined from Au (Fig. 12a). And it is reported that the highest occupied molecular orbital (HOMO) and lowest unoccupied molecular orbital (LUMO) energy levels of [Ru(bpy)$_3$]Cl$_2$ are 5.68 and 3.19 eV respectively with respect to the vacuum level.[147] Thus electrons transfer from LUMO of [Ru(bpy)$_3$]Cl$_2$ to the Fermi level of Co$_1$–G for the subsequent reduction of CO$_2$ (Fig. 12c). Meanwhile, the energy gap near 0 eV between the E_F

and VB edge exhibited by the valence-band (VB) spectrum signifies the zero-bandgap feature of Co$_1$–G (Fig. 12b). Wang *et al.* claimed Pt SACs (PtSACs/C) synthesized by the electroplating strategy with the assistance of graphene oxide membrane (GOM) blocking the diffuse and aggregation of Pt ions in a H-cell.[148] The work function and energy gap between the E_F and VB edge of PtSACs/C are 4.2 eV and ~0 eV respectively with the incident photon energy of 40.0 eV (Fig. 12d and e), also suggesting the zero-bandgap trait. Combining UV-vis diffuse reflectance spectrum, the photocatalytic HER process is illustrated in Fig. 12f.

So benefit from getting information of total catalysts rather than individual elements, the ability of getting and losing electrons of SACs can be evaluated by UPS straightly, which is closely connected with local environments and plays a significant role in unravelling the reactive mechanisms. Otherwise like XPS, the impact of UHV on the interface of catalysts cannot be ignored.

2.2.3 Depth detection of elementary distribution by SRPES. It is comprehensible that X-ray with different wavenumbers has
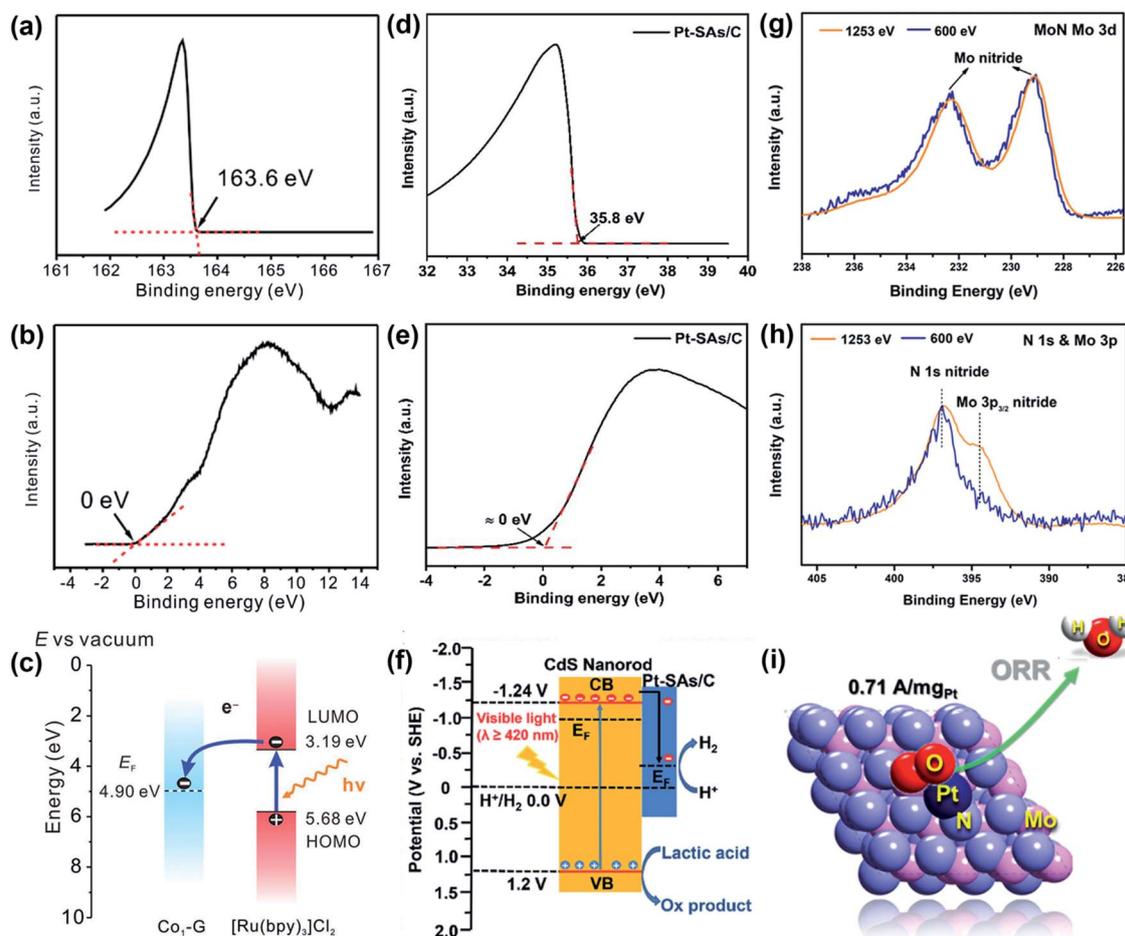

Fig. 12 (a, b) Secondary electron cutoff spectrum (a) and VB spectrum (b) of Co$_1$-G; (c) schematic energy-level diagram. Reprinted with permission from ref. 146. Copyright 2018, WILEY-VCH Verlag GmbH & Co. KGaA, Weinheim. (d, e) Secondary electron cutoff spectrum(d) and VB spectrum (e) of PtSAs/C; (f) the photocatalytic mechanism. Reproduced from ref. 148 with permission from the Royal Society of Chemistry. (g, h) Mo 3d (g) and N 1s (h) spectra of MoN at photon energies of 1253 and 600 eV; (i) optimized structure for Pt supported on MoN. Reprinted with permission from ref. 150. Copyright 2020, American Chemical Society.

5782 | *J. Mater. Chem. A*, 2022, **10**, 5771–5791

This journal is © The Royal Society of Chemistry 2022

element-specific detection sensitivity and depth of penetration. It means the difference of elementary distribution between surface and sub-surface can be described by SRPES, in which there is hidden information about local coordinate environments.[149] For instance, Li *et al.* achieved atomically dispersed Pt anchored on face-centered cubic(fcc)-structured MoN by the wet-impregnation and NH_3-activation method.[150] SRPES was employed to understand the difference between bulk and surface of MoN with photon energies of 1253 and 600 eV. Although Mo 3d spectrum keeps invariable at both conditions (Fig. 12g), the shoulder peak representing Mo 3p almost disappears in the N 1s and Mo 3p spectra at 600 eV (Fig. 12h), indicating N atoms are enriched on the surface. Hence Pt SAs tend to be coordinated with surficial N rather than Mo, agreeing well with EXAFS results (Fig. 12i). But the studies about the depth detection model for SACs are still scarce as far as we know. The fact is that statistical signals coming from both bulk and surface are obtained while employing high-energy X-ray as incident light, which hinders the extraction of valuable responses.

In brief, SRPES points at electronic states of target elements as a surface-sensitive technique, which is complementary to XAS for SACs. On account of the bother of UHV, synchrotron-radiation NAP-XAP or AP-XPS with the controllable atmosphere and temperature develops flourishingly, especially in the thermocatalytic field. *In situ* and *operando* NAP-XPS are employed to track the pressure- and temperature-dependent relationships between local environments of SACs and gas reactants in real time, disclosing the reactive steps farther. On the other hand, synchrotron-radiation UPS incorporating UV-vis diffuse reflectance spectra and DFT calculations gives detailed information of the electronic flowing direction. And the adjustable energy feature of synchrotron radiation light makes depth detection of elementary distribution possible. However, it should not be ignored that rigorous service conditions of PES confine the applications of other outfields, which need to be optimized.

2.3 SR-FTIR

SR-FTIR is a significant part of synchrotron-radiation methodologies on account of the convenience for observing intermediates and adsorbates in catalytic processes.[151] Compared with conventional light sources, the focused beam of infrared light generated by synchrotron radiation is smaller in size and brighter, significantly optimizing the SNR.[152] Moreover, the superior expansibility of SR-FTIR renders it meeting various demands involving *in situ*, *operando*, low-temperature, *etc.* (Fig. 13a)[153]

Generally, local environments of catalysts have a deep influence on probing molecular bonding types and vibration modes. So the structural features of SACs can be deduced from adsorption behaviours. For instance, synchrotron-radiation CO-probing DRIFTS results of Pd SAs, H_2-treated Pd SAs and Pd NPs denoted as Pd-SAs/3DOM-CeO_2, Pd-SAs/3DOM-CeO_2-H_2 and Pd-NPs/3DOM-CeO_2 respectively, were contrasted by Tao and coworkers.[154] The sharp peak at 2153 cm^{-1} belongs to strhing variation of linear-adsorbed CO on Pd SAs, indicating atomic dispersion in Pd-SAs/3DOMCeO_2 (Fig. 13b). An obvious shift of this sharp peak and another broad peak assigned to the linear-adsorbed CO on Pd clusters are observed, suggesting the clustering and reduction of Pd after H_2 treatment. Distinctly, two broad bands located at 1890 and 2090 cm^{-1} are accord with the threefold-hollow-adsorbed CO and minor linear-adsorbed CO on Pd NPs of Pd-NPs/3DOM-CeO_2 respectively. Then to insight
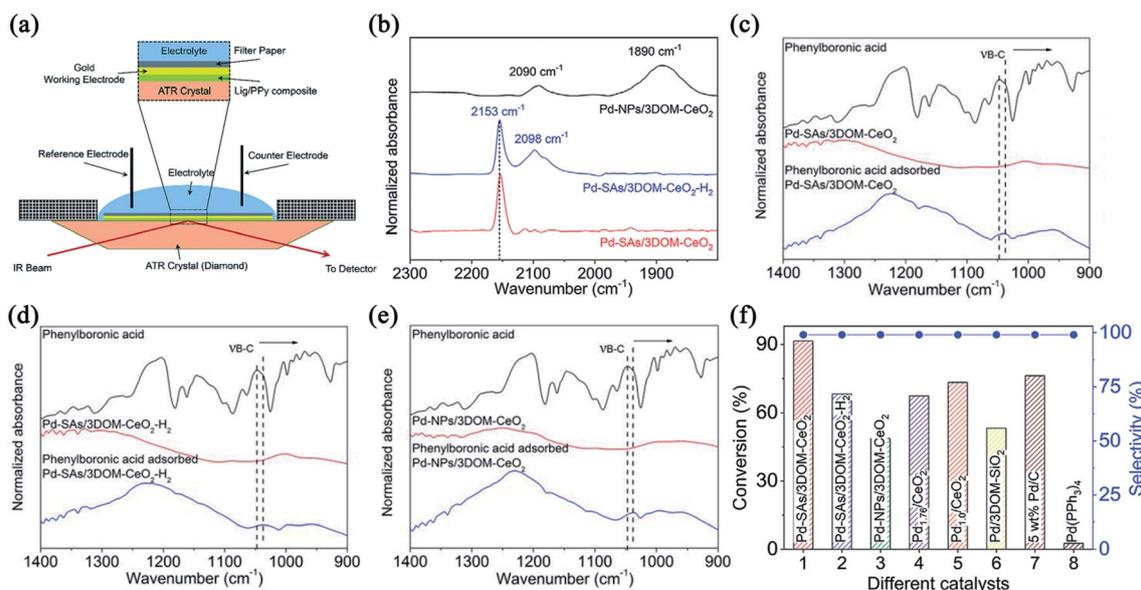

Fig. 13 (a) Schematic representation of the *in situ* FTIR setup. Reproduced from ref. 153 with permission from the Royal Society of Chemistry. (b) CO-probing spectra of Pd-SAs/3DOM-CeO_2, Pd-SAs/3DOM-CeO_2-H_2 and Pd-NPs/3DOM-CeO_2; (c–e) FTIR spectra of phenylboronic acid adsorbed on these catalysts; (f) catalytic performance toward the Suzuki reaction of iodobenzene and phenylboronic acid. Reprinted with permission from ref. 154. Copyright 2020, WILEY-VCH GmbH.

This journal is © The Royal Society of Chemistry 2022

J. Mater. Chem. A, 2022, **10**, 5771–5791 | **5783**

into the positive role of Pd SAs, IR spectra were collected after the chemical adsorption of phenylboronic acid. The B–C stretching vibration peak at ~1050 cm^{-1} exhibits more down-shifts in Pd-SAs/3DOM-CeO$_2$ than other two references, indicating that high-valence isolated Pd sites are more competent to activate phenylboronic acid in transmetalation step of Suzuki coupling reactions (Fig. 13c–e). Pd-SAs/3DOM-CeO$_2$ exhibits superior conversion efficiency and selectivity towards Suzuki reactions, surpassing Pd NPs (Fig. 13f).

Moreover, SR-FTIR method can approach the requirements of *in situ* and *operando* methods.[155,156] They are able to provide fingerprint identification of real-time active groups, which is of great concern in the hypothesis of reactive pathways for SACs. It is reported that the adsorbed OOH, O and OH intermediates detected by *in situ* SR-FTIR spectra present in the Cu-catalytic ORR reaction, which agreed well with the proposed

mechanism.[157] On the other hand, central metal atoms and neighbouring ligand atoms usually take synergetic effect in catalytic reactions. This effect can be distinguished by *in situ* and *operando* SR-FTIR, helpfully understanding the relation between local environments and catalytic performances. For instance, Su *et al.* reported isolated single-atom Ni supported on MOFs-derived carbon nitride (Ni$_1$–NC) through ion-exchange and node-confined procedures.[158] Two new absorption bands at 908 and 3465 cm^{-1} in *operando* SR-FTIR spectra are assigned to surface adsorbed O intermediate species and O–H from adsorbed water molecules respectively at the applied potentials (Fig. 14a and b). The relation between intensity and voltages was plotted in Fig. 14c. The rising part represents the evident accumulation of adsorbed O intermediates and adsorbed H$_2$O species at the solid–liquid interfaces (SLEIs) under the preliminary voltages, promoting the rate-determining step of O–O
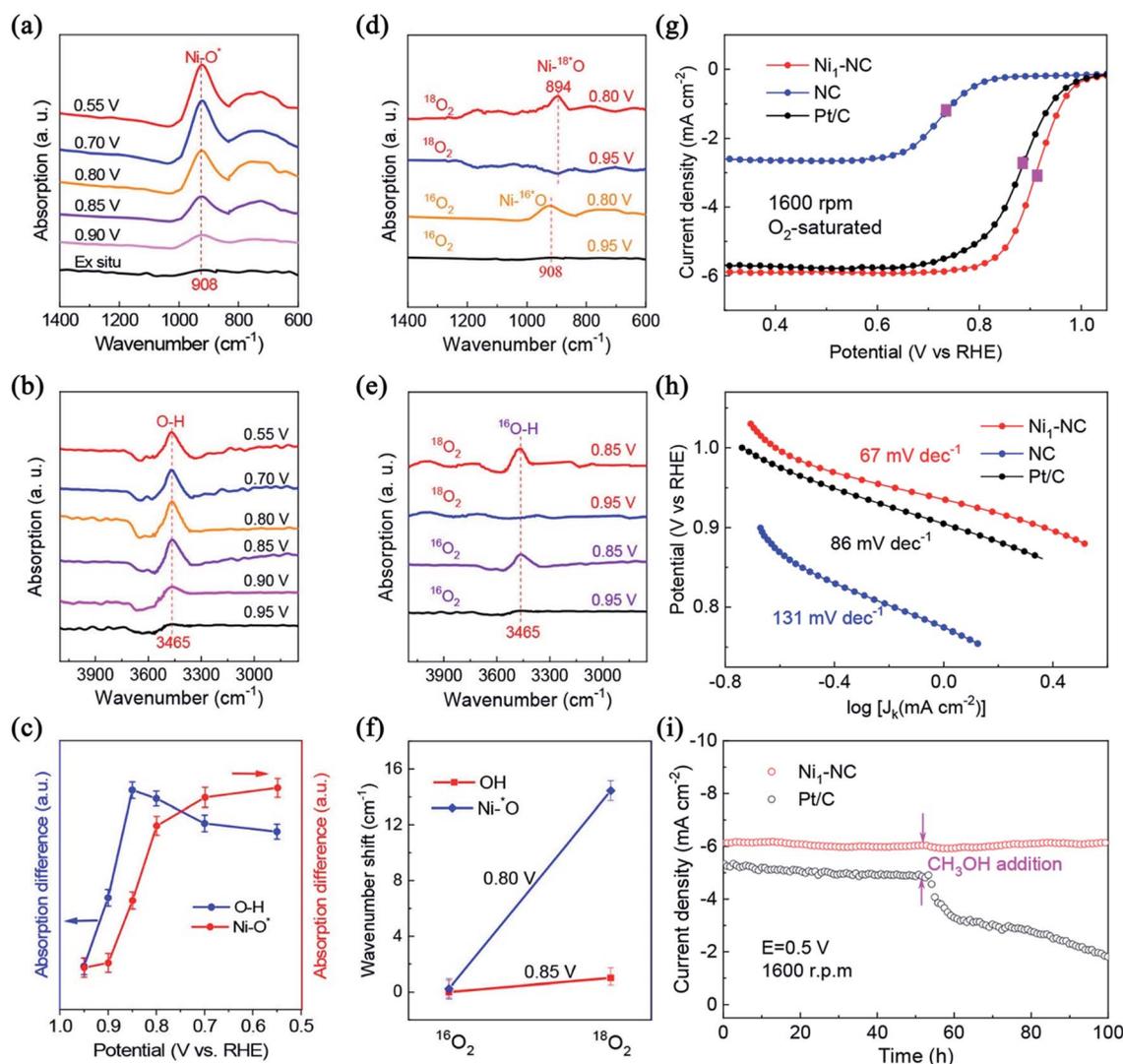

Fig. 14 (a, b) *Operando* IR measurements of Ni$_1$–NC during the ORR process; (c) signals at 3465 and 908 cm^{-1} *versus* the potential; (d, e) isotope-labeling *operando* spectroscopy for Ni$_1$–NC under various potentials; (f) the corresponding wavenumber shift; (g) linear sweep voltammograms (LSVs) at 1600 rpm; (h) Tafel plots; (i) methanol tolerance tests at 0.5 V *versus* RHE. Reprinted with permission from ref. 158. Copyright 2020, American Chemical Society.

5784 | *J. Mater. Chem. A*, 2022, **10**, 5771–5791

This journal is © The Royal Society of Chemistry 2022

dissociation in ORR to some extent. Keeping decreasing potentials *versus* RHE, the intensity at 908 cm^{-1} reaches an approximate saturation plateau while ~3465 cm^{-1} presents a decline, elucidating the synergistic effect between hydroxyl on N/C sites adjacent to the Ni active centers and crucial adsorbed O intermediates promoted by Ni$_1$N$_2$ active sites. In isotope-labeling *operando* SR-FTIR with ^{18}O$_2$ and H$_2$^{16}O, the shift of O–Ni and unchanged O–H confirm they originate from O$_2$ reactants and H$_2$O in electrolyte respectively (Fig. 14d–f). *Operando* XAFS and SR-FTIR analyses confirmed the formation of near-free isolated-zigzag Ni$_1$$^{(2-\delta)+}N_2$ active sites, which provide excellent ORR activity and durability by facilitating the adsorption and dissociation of O$_2$ into crucial *O intermediates (Fig. 14g–i).

Besides, SR-FTIR spectra fit other peculiar testing demands including low-temperature reflection and variable angle reflection.[74] For instance, Ye *et al.* precisely tuned the number of Fe atoms to fabricate Fe SAs, Fe$_2$ and Fe$_3$ clusters anchored on N-doped carbon marked as Fe$_x$–N–C by pre-encapsulation and pyrolysis schedules.[159] In low-temperature FTIR spectroscopies (LT-FTIR) after exposing catalysts to O$_2$ for 10 min to ensure complete O$_2$ adsorption, broad peaks located at 1200–1350 cm^{-1} for Fe$_1$–N–C and 800–1000 cm^{-1} for Fe$_2$ and Fe$_3$–N–C are attributed to the vibrations of adsorbed superoxo-like (akin to Fe–O–O) and peroxo-like (akin to Fe–O–O–Fe) O$_2$ species respectively. This indicates that the number of Fe atoms in clusters can really alter O$_2$ adsorption configurations, in consistence with theoretical calculation results.

Conclusively, the adsorption-dissociation behaviors are regulated extensively by well-defined isolated metal sites with diverse local environments. *In situ* and *operando* identification of reactive configurations is vital to put forward accurate elementary reaction pathways of SACs. Specific requirements like low temperature and molecular probing are also able to be approached by SR-FTIR. However, the semi-quantitative character of IR blocks the progressive utilization in plotting the formula between the accumulation of intermediates and catalytic performance. Meanwhile, the peak intensity and width are related to not only the concentrations but also the vibration type of the bonds. The overlaps in wavenumbers of some bonds are also inseparable and inevitable.

3. Summary and perspective

Coupled microscopy and spectroscopy methods, a thorough characterization system for SACs has been built in the past decade. The combination of synchrotron radiation-based multitechniques (SRMS) has proved to be powerful in identifying the diverse local environments of isolated sites.[160] This work summarized the advantages and limitations of existing synchrotron-radiation measurements including XAS, SRPES and SR-FTIR. It is worth noting that aforesaid methods cannot replace each other. The reasonable reaction mechanisms are only proposed by the comprehensive knowledge and analysis of all experimental and theoretical results. Based on this, respective roles of synchrotron-radiation tests acting in the studies of SACs and relevant outlooks are described as following.

3.1 Oxidation states

Although the dispersion degree of confined metal atoms should be evaluated straightly by the high-angle annular dark-field scanning transmission electron microscopy (HAADF-STEM), the elementary electropositivity confirmed by bulk-sensitive XANES and surface-sensitive XPS is also efficient. Meanwhile, *ex situ* XANES spectra detecting beginning and ending states of center and assistant atoms have the ability in deciphering partial mechanisms concerned with irreversible redox activation, electronic interaction and corrosion resistance, *etc.*[92] On the other hand, the valence change of center atoms is strongly related to the redox-involved reaction performance of SACs. Some reversible or instantaneous intermediate states can only be investigated by *in situ/operando* XANES and NAP-XPS. The flourishing development of computational analysis of *in situ* XAS results offers the elaborate explanation of the evolution of isolated sites influenced by various outfields.[95] *Operando* NAP-XPS is naturally suitable to deal with gas-involved courses through building the relationship between gas molecules and active sites, for thermocatalysis in particularly.

3.2 Coordinate configurations

There is no doubt that the coordinated atoms and bonding types have a deep impact on catalytic activity when SAs are acknowledged as the reactive origin. EXAFS has unique advantages in recognizing the local coordinate environments. The coordinate number and bond length are obtained by EXAFS fitting to distinguish diverse local environments. Moreover, EXAFS satisfies the demands of *in situ* and *operando* measurements that are performed to unravel the evolution of chemical environments and structure–property relationship of SACs. Besides, depth detection of elementary distribution by SRPES can give a longitudinal distribution of atomic concentrations in a certain depth range, hinting the bonding modes between metal and ligand atoms.[150]

3.3 Support coupling effect

The electronic structures and stability of catalytically active sites are regulated by miscellaneous well-defined supports. Understanding the electronic metal–support interaction is of great concern in conducting mechanism researches. For classical structure of that transition metal is bonded with C, N, O, S, *etc.*, soft XAS takes effect in the investigation of orbital hybridization and support coupling effect. Kinds of ligands such as pyridinic N, pyrrolic N and graphitic N, can be distinguished by the peak fitting of soft XAS, which is deeply connected with the adsorption energy of specific intermediates.[119]

3.4 Intermediates and adsorption behaviors

The interaction between reagents and adsorbed sites was deduced indirectly from the change of oxidation states by XANES and NAP-XPS before. However, the direct observation of adsorption kinds on SACs can only be achieved by *in situ* and *operando* SR-FTIR in the family of synchrotron-radiation techniques. The evolution of intermediate states is illustrated by their unique

This journal is © The Royal Society of Chemistry 2022

J. Mater. Chem. A, 2022, **10**, 5771–5791 | **5785**

stretching or bending vibration. In addition, UPS explains the interactions between reagents and catalysts through the gaining/losing-electron ability evaluated by the work function.

Despite the unprecedented progress has been achieved in synchrotron-radiation *ex/in situ* and *operando* studies, there are multiple factors hindering more comprehensive acknowledgement of SACs-catalytic processes. The aspects that need to be further modified for synchrotron-radiation techniques are listed as following to expect to gain a coherent picture of the structure–property relationship for SACs in the not-too-distant future.

(1) The equipment covering detector, *in situ* cell, *etc.* and their relevant installation interval should be standardized and optimized to decrease the time of collecting spectra and increase SNR. For example, low background of XAS provides more possibility to identify slight changes in oxidation states and coordinate environments, or increase the sensitivity for some single-atom model catalysts with trace metal. Especially for soft XAS, the lack of in situ and operando measurements in SACs makes it imperative to design reasonable metrical procedures. For NAP-XPS, the applied atmosphere pressure region should be extended to weaken the near-ambient influence on catalytic structures.

(2) The more convincing data processing methods should be proposed combing theoretical calculation. As shown in chapter two, the XAS analysis is not limited to the contrast of the white line in XANES and least-square fitting in EXAFS any more. The more reasonable structural models are built by coupling of experimental and theoretical spectra. Linear combination fitting (LCF) results using advisable reference spectra can match well with the experimental results, which gives an interpretation of the evolution of probed catalytically active atoms.[95] And the species of ligands can be elucidated by resolving adsorption bands in soft XAS spectra. Thus it can be realized that there is considerable progress in handling methods of XAS. And we have reasons to believe that well-disposed XAS will play a more crucial role in the characterization of SACs.

(3) Extending the kind of outfields that can be performed under work conditions is impending. Restricted by the features of diverse techniques, synchrotron-radiation methods usually have their own comfort zones for outfields applying to *in situ* and *operando* measurements. For example, NAP-XPS is naturally suitable for thermocatalytic reactions while the employment in electrocatalysis and photocatalysis is relatively fewer for SACs. *In situ* soft XAS has already been performed for bulk catalysts in electrocatalytic processes, but not for SACs.

(4) The characterization of SACs usually needs a comprehensive system encompassing multiple unique techniques. Thus, more powerful synchrotron-radiation methods need to be exploited for SACs to enrich this characterization family. Synchrotron-radiation X-ray emission spectroscopy (XES) relying on the ionization of electrons and detecting the intensity of the fluorescence at the maintained incident X-ray photon energy, is potential in this case. Valence-to-core XES (VTC-XES) of 3d transition metals can be used to distinguish neighboring ligand atoms of SACs such as C, N, O, S, *etc.*161 For example, it is reported that the transitions of local environments from isolated Mo–O species to partially carburized MoC_xO_y and

totally carburized MoC_x occur during methane dehydroaromatization (MDA), confirmed by characteristic $K_{\beta''}$ peak of Mo oxide (Fig. 15a).[162] On the other hand, the typical long-range disorder property disables XRD and small-angle X-ray scattering (SAXS) for investigating the SACs under the static state. But *in situ/operando* XRD and SAXS take effect in tracking the dynamic evolution of isolated sites and supports, which is efficient for evaluating catalytic stability and unveiling clustering processes. For instance, Liu *et al.* chose single-site Co in a well-defined brookite TiO_2 (210) nanorod (Co-TiO$_2$) as a model catalyst for OER. *In situ* synchrotron-radiation XRD (SRXRD) shows no phase transition for TiO_2 support and metal segregation for Co (Fig. 15d), suggesting the good stability.[163] And it is reported that obvious agglomeration can be observed through a signal enhancement in the q range around 0.1 Å^{-1} in *operando* grazing-incidence SAXS (GISAXS) while calcinating Pt clusters (Pt$_{24}$/SiO$_2$/Si) from 50 to 200 °C in H$_2$ (Fig. 15b and c).[164] Thus it is convincing that SAXS can play a vital part in identifying real sites in the processes of reduction and clustering of SACs.[165,166] However, the applications of XES, XRD and SAXS are still scarce in SACs to the best of our knowledge.
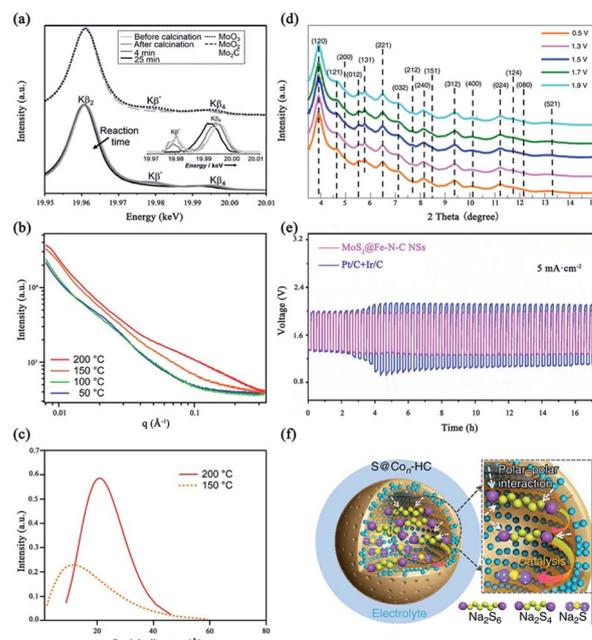

Fig. 15 (a) Bottom: K_{β} emission bands recorded before and after calcination, and after quenching of the MDA reaction at 4 min and 25 min; the Inset is background-removed VTC-XES; top: spectra of MoO$_3$, Mo$_2$C, and MoO$_2$ references. Reprinted with permission from ref. 162. Copyright 2016, Wiley-VCH Verlag GmbH & Co. KGaA. (b) GISAXS intensity change of Pt$_{24}$/SiO$_2$/Si during the heating cycle from 50 to 200 °C in H$_2$; (c) fitted particle size distributions. Reprinted with permission from ref. 164. Copyright 2017, American Chemical Society. (d) *In situ* SRXRD patterns of Co−TiO$_2$ nanorod catalysts under the OER conditions. Reprinted with permission from ref. 163. Copyright 2021, Springer Nature. (e) The stability curve of ZABs. Reprinted with permission from ref. 170. Copyright 2021, National Academy of Sciences. (f) Schematic illustrations of electrode reaction mechanism. Reprinted with permission from ref. 171. Copyright 2018, Springer Nature.

5786 | *J. Mater. Chem. A*, 2022, **10**, 5771–5791

This journal is © The Royal Society of Chemistry 2022

It is worth noting that the applications of SACs have been extended to the whole courses of energy-storage and conversion. Recently, SACs in metal-air and lithium/sodium-sulfur batteries, proton exchange membrane full cells (PEMFC), *etc.*, have attracted great attention.[167–169] And synchrotron-radiation spectroscopies also take effect in these conditions. Yan *et al.* put forward a facile strategy for crafting wrinkled MoS_2/N-doped carbon core/shell nanospheres interfaced with single Fe atoms for wearable, high-capacity, and cycling-stability aqueous zinc-air battery (ZABs) (Fig. 15e).[170] The Fe–N_4 configuration is confirmed by the fitting of FT-EXAFS. Zhang *et al.* employed sulfur encapsulated Co SAs and clusters anchored on hollow carbon nanospheres (S@Co_n-HC) as the cathode of room-temperature sodium-sulfur battery (RT-Na/S).[171] The transition among S, Na_2S_x, Na_2S_4, Na_2S_2 and Na_2S is observed by *in situ* SRXRD, suggesting the electrocatalytic effects of atomic cobalt (Fig. 15f).

In summary, the development of SACs is tightly connected with progressive synchrotron-radiation *ex/in situ* and *operando* spectroscopies. Particularly, an unambiguous picture of the structure–activity relationship of SACs will be built by tighter combination of multiple *in situ* and *operando* synchrotron-radiation technologies. And the further developments of them have to reconcile the depth and breadth. That is, it is paratactic for optimizing data quality of one method and extending the characterization families of SACs. Furthermore, the catalytic performances are usually tailored by electronic interactions, geometric effects, local coordinate configurations, *etc.* The comprehensive cognitions from synchrotron-radiation spectroscopies, electron microscopies and other important methods are instructive for SACs in either tracking the origin of activities or providing guidelines for optimization designs.

Conflicts of interest

There are no conflicts to declare.

Acknowledgements

References

1 S. C. Doney, V. J. Fabry, R. A. Feely and J. A. Kleypas, *Annu. Rev. Mar. Sci.*, 2009, **1**, 169–192.

2 U. Büntgen, P. J. Krusic, A. Piermattei, D. A. Coomes, J. Esper, V. S. Myglan, A. V. Kirdyanov, J. J. Camarero, A. Crivellaro and C. Körner, *Nat. Commun.*, 2019, **10**, 2171.

3 P. Veers, K. Dykes, E. Lantz, S. Barth, C. L. Bottasso, O. Carlson, A. Clifton, J. Green, P. Green, H. Holttinen, D. Laird, V. Lehtomäki, J. K. Lundquist, J. Manwell, M. Marquis, C. Meneveau, P. Moriarty, X. Munduate, M. Muskulus, J. Naughton, L. Pao, J. Paquette, J. Peinke, A. Robertson, J. Sanz Rodrigo, A. M. Sempreviva, J. C. Smith, A. Tuohy and R. Wiser, *Science*, 2019, **366**, eaau2027.

4 Y. Zhao, C. Ding, J. Zhu, W. Qin, X. Tao, F. Fan, R. Li and C. Li, *Angew. Chem., Int. Ed.*, 2020, **132**, 9740–9745.

5 R. F. Service, *Science*, 2019, **365**, 108.

6 C. Wang, S. Chen, H. Xie, S. Wei, C. Wu and L. Song, *Adv. Energy Mater.*, 2019, **9**, 1802977.

7 R. Liu and C. Streb, *Adv. Energy Mater.*, 2021, **11**, 2101120, DOI: 10.1002/aenm.202101120.

8 Z. Kou, W. Zang, W. Pei, L. Zheng, S. Zhou, S. Zhang, L. Zhang and J. Wang, *J. Mater. Chem. A*, 2020, **8**, 3071–3082.

9 Y. Zhou, Z. Xie, J. Jiang, J. Wang, X. Song, Q. He, W. Ding and Z. Wei, *Nat. Catal.*, 2020, **3**, 454–462.

10 N. Zhang, X. Feng, D. Rao, X. Deng, L. Cai, B. Qiu, R. Long, Y. Xiong, Y. Lu and Y. Chai, *Nat. Commun.*, 2020, **11**, 4066.

11 M. Luo, Z. Zhao, Y. Zhang, Y. Sun, Y. Xing, F. Lv, Y. Yang, X. Zhang, S. Hwang, Y. Qin, J. Y. Ma, F. Lin, D. Su, G. Lu and S. Guo, *Nature*, 2019, **574**, 81–85.

12 S. Cao, Y. Wang, B. Zhu, G. Xie, J. Yu and J. R. Gong, *J. Mater. Chem. A*, 2020, **8**, 7671–7676.

13 X. Pan, F. Jiao, D. Miao and X. Bao, *Chem. Rev.*, 2021, **121**, 6588–6609.

14 H. Jiang, Q. He, X. Li, X. Su, Y. Zhang, S. Chen, S. Zhang, G. Zhang, J. Jiang, Y. Luo, P. M. Ajayan and L. Song, *Adv. Mater.*, 2019, **31**, 1805127.

15 H. Wang, Z. N. Chen, D. Wu, M. Cao, F. Sun, H. Zhang, H. You, W. Zhuang and R. Cao, *J. Am. Chem. Soc.*, 2021, **143**, 4639–4645.

16 D. Liu, X. Li, S. Chen, H. Yan, C. Wang, C. Wu, Y. A. Haleem, S. Duan, J. Lu, B. Ge, P. M. Ajayan, Y. Luo, J. Jiang and L. Song, *Nat. Energy*, 2019, **4**, 512–518.

17 S. Yang, Q. He, C. Wang, H. Jiang, C. Wu, Y. Zhang, T. Zhou, Y. Zhou and L. Song, *J. Mater. Chem. A*, 2018, **6**, 11281–11287.

18 A. Wang, J. Li and T. Zhang, *Nat. Rev. Chem.*, 2018, **2**, 65–81.

19 Z. Zeng, Y. Su, X. Quan, W. Choi, G. Zhang, N. Liu, B. Kim, S. Chen, H. Yu and S. Zhang, *Nano Energy*, 2020, **69**, 104409.

20 L. Zhang, R. Long, Y. Zhang, D. Duan, Y. Xiong, Y. Zhang and Y. Bi, *Angew. Chem., Int. Ed.*, 2020, **59**, 6224–6229.

21 H. Jin, X. Liu, S. Chen, A. Vasileff, L. Li, Y. Jiao, L. Song, Y. Zheng and S. Z. Qiao, *ACS Energy Lett.*, 2019, **4**, 805–810.

22 Y. Shang, X. Xu, B. Gao, S. Wang and X. Duan, *Chem. Soc. Rev.*, 2021, **50**, 5281–5322.

23 P. Zhou, F. Lv, N. Li, Y. Zhang, Z. Mu, Y. Tang, J. Lai, Y. Chao, M. Luo, F. Lin, J. Zhou, D. Su and S. Guo, *Nano Energy*, 2019, **56**, 127–137.

24 W. H. Lai, L. F. Zhang, W. B. Hua, S. Indris, Z. C. Yan, Z. Hu, B. Zhang, Y. Liu, L. Wang, M. Liu, R. Liu, Y. X. Wang,

This journal is © The Royal Society of Chemistry 2022

J. Mater. Chem. A, 2022, **10**, 5771–5791 | **5787**

J. Z. Wang, Z. Hu, H. K. Liu, S. L. Chou and S. X. Dou, *Angew. Chem., Int. Ed.*, 2019, **58**, 11868–11873.

25 X. Zheng, J. Tang, A. Gallo, J. A. Garrido Torres, X. Yu, C. J. Athanitis, E. M. Been, P. Ercius, H. Mao, S. C. Fakra, C. Song, R. C. Davis, J. A. Reimer, J. Vinson, M. Bajdich and Y. Cui, *Proc. Natl. Acad. Sci. U. S. A.*, 2021, **118**, e2101817118.

26 H. Y. Jeong, M. Balamurugan, V. S. K. Choutipalli, E. S. Jeong, V. Subramanian, U. Sim and K. T. Nam, *J. Mater. Chem. A*, 2019, **7**, 10651–10661.

27 W. Xiong, H. Li, H. Wang, J. Yi, H. You, S. Zhang, Y. Hou, M. Cao, T. Zhang and R. Cao, *Small*, 2020, **16**, 2003943.

28 B. Han, Y. Gao, Y. Huang, W. Xi, J. Xu, J. Luo, H. Qi, Y. Ren, X. Liu, B. Qiao and T. Zhang, *Angew. Chem., Int. Ed.*, 2020, **132**, 11922–11927.

29 T. Zhang, X. Han, H. Yang, A. Han, E. Hu, Y. Li, X. Yang, L. Wang, J. Liu and B. Liu, *Angew. Chem., Int. Ed.*, 2020, **132**, 12153–12159.

30 B. Chen, T. Wang, S. Zhao, J. Tan, N. Zhao, S. P. Jiang, Q. Zhang, G. Zhou and H. M. Cheng, *Adv. Mater.*, 2021, **33**, 2007090.

31 X. Xiao, Y. Gao, L. Zhang, J. Zhang, Q. Zhang, Q. Li, H. Bao, J. Zhou, S. Miao, N. Chen, J. Wang, B. Jiang, C. Tian and H. Fu, *Adv. Mater.*, 2020, **32**, 2003082.

32 H. Wang, Q. Wang, Y. Cheng, K. Li, Y. Yao, Q. Zhang, C. Dong, P. Wang, U. Schwingenschlögl, W. Yang and X. X. Zhang, *Nano Lett.*, 2012, **12**, 141–144.

33 T. He, S. Chen, B. Ni, Y. Gong, Z. Wu, L. Song, L. Gu, W. Hu and X. Wang, *Angew. Chem., Int. Ed.*, 2018, **130**, 3551–3556.

34 P. Zhou, N. Li, Y. Chao, W. Zhang, F. Lv, K. Wang, W. Yang, P. Gao and S. Guo, *Angew. Chem., Int. Ed.*, 2019, **58**, 14184–14188.

35 J. Han, H. Bao, J. Q. Wang, L. Zheng, S. Sun, Z. L. Wang and C. Sun, *Appl. Catal., B*, 2021, **280**, 119411.

36 J. Gao, H. b. Yang, X. Huang, S. F. Hung, W. Cai, C. Jia, S. Miao, H. M. Chen, X. Yang, Y. Huang, T. Zhang and B. Liu, *Chem*, 2020, **6**, 658–674.

37 K. Qi, M. Chhowalla and D. Voiry, *Mater. Today*, 2020, **40**, 173–192.

38 Q. He, Y. Wan, H. Jiang, Z. Pan, C. Wu, M. Wang, X. Wu, B. Ye, P. M. Ajayan and L. Song, *ACS Energy Lett.*, 2018, **3**, 1373–1380.

39 J. Zhang, X. Wu, W. C. Cheong, W. Chen, R. Lin, J. Li, L. Zheng, W. Yan, L. Gu, C. Chen, Q. Peng, D. Wang and Y. Li, *Nat. Commun.*, 2018, **9**, 1002.

40 Y. Lu, T. Liu, C. L. Dong, Y. C. Huang, Y. Li, J. Chen, Y. Zou and S. Wang, *Adv. Mater.*, 2021, **33**, 2007056.

41 J. Mao, J. Yin, J. Pei, D. Wang and Y. Li, *Nano Today*, 2020, **34**, 100917.

42 S. Luo, L. Zhang, Y. Liao, L. Li, Q. Yang, X. Wu, X. Wu, D. He, C. He, W. Chen, Q. Wu, M. Li, E. J. M. Hensen and Z. Quan, *Adv. Mater.*, 2021, **33**, 2008508.

43 A. M. Abdel Mageed, B. Rungtaweevoranit, M. Parlinska-Wojtan, X. Pei, O. M. Yaghi and R. J. Behm, *J. Am. Chem. Soc.*, 2019, **141**, 5201–5210.

44 Y. Zhu, X. Yang, C. Peng, C. Priest, Y. Mei and G. Wu, *Small*, 2021, **17**, 2005148.

45 J. Ban, X. Wen, H. Xu, Z. Wang, X. Liu, G. Cao, G. Shao and J. Hu, *Adv. Funct. Mater.*, 2021, **31**, 2010472.

46 Z. Song, L. Zhang, K. Doyle-Davis, X. Fu, J. L. Luo and X. Sun, *Adv. Energy Mater.*, 2020, **10**, 2001561.

47 P. Peng, L. Shi, F. Huo, C. Mi, X. Wu, S. Zhang and Z. Xiang, *Sci. Adv.*, 2019, **5**, eaaw2322.

48 Y. Zhang, L. Jiao, W. Yang, C. Xie and H. L. Jiang, *Angew. Chem., Int. Ed.*, 2021, **60**, 7607–7611.

49 J. Hulva, M. Meier, R. Bliem, Z. Jakub, F. Kraushofer, M. Schmid, U. Diebold, C. Franchini and G. S. Parkinson, *Science*, 2021, **371**, 375–379.

50 W. Guo, S. Liu, X. Tan, R. Wu, X. Yan, C. Chen, Q. Zhu, L. Zheng, J. Ma, J. Zhang, Y. Huang, X. Sun and B. Han, *Angew. Chem., Int. Ed.*, 2021, **60**, 21979.

51 C. Tang, L. Chen, H. Li, L. Li, Y. Jiao, Y. Zheng, H. Xu, K. Davey and S. Z. Qiao, *J. Am. Chem. Soc.*, 2021, **143**, 7819–7827.

52 S. Li, S. Zhao, X. Lu, M. Ceccato, X. M. Hu, A. Roldan, J. Catalano, M. Liu, T. Skrydstrup and K. Daasbjerg, *Angew. Chem., Int. Ed.*, 2021, **60**, 22826–22832.

53 Q. Wang, X. Huang, Z. L. Zhao, M. Wang, B. Xiang, J. Li, Z. Feng, H. Xu and M. Gu, *J. Am. Chem. Soc.*, 2020, **142**, 7425–7433.

54 L. S. Zhang, X. H. Jiang, Z. A. Zhong, L. Tian, Q. Sun, Y. T. Cui, X. Lu, J. P. Zou and S. L. Luo, *Angew. Chem., Int. Ed.*, 2021, **60**, 21751–21755.

55 S. Wang, P. Zhou, L. Zhou, F. Lv, Y. Sun, Q. Zhang, L. Gu, H. Yang and S. Guo, *Nano Lett.*, 2021, **21**, 4262–4269.

56 C. Xia, Y. Qiu, Y. Xia, P. Zhu, G. King, X. Zhang, Z. Wu, J. Y. T. Kim, D. A. Cullen, D. Zheng, P. Li, M. Shakouri, E. Heredia, P. Cui, H. N. Alshareef, Y. Hu and H. Wang, *Nat. Chem.*, 2021, **13**, 887–894.

57 Y. Xiong, W. Sun, P. Xin, W. Chen, X. Zheng, W. Yan, L. Zheng, J. Dong, J. Zhang, D. Wang and Y. Li, *Adv. Mater.*, 2020, **32**, 2000896.

58 N. Zhang, X. Zhang, L. Tao, P. Jiang, C. Ye, R. Lin, Z. Huang, A. Li, D. Pang, H. Yan, Y. Wang, P. Xu, S. An, Q. Zhang, L. Liu, S. Du, X. Han, D. Wang and Y. Li, *Angew. Chem., Int. Ed.*, 2021, **60**, 6170–6176.

59 W. Chen, C. Xie, Y. Wang, Y. Zou, C. L. Dong, Y. C. Huang, Z. Xiao, Z. Wei, S. Du, C. Chen, B. Zhou, J. Ma and S. Wang, *Chem*, 2020, **6**, 2974–2993.

60 K. Codling, *Rep. Prog. Phys.*, 1973, **36**, 541–624.

61 D. D. Babu, Y. Huang, G. Anandhababu, X. Wang, R. Si, M. Wu, Q. Li, Y. Wang and J. Yao, *J. Mater. Chem. A*, 2019, **7**, 8376–8383.

62 Q. He, J. H. Lee, D. Liu, Y. Liu, Z. Lin, Z. Xie, S. Hwang, S. Kattel, L. Song and J. G. Chen, *Adv. Funct. Mater.*, 2020, **30**, 2000407.

63 W. Xu, D. Cao, O. A. Moses, B. Sheng, C. Wu, H. Shou, X. Wu, S. Chen and L. Song, *Nano Res.*, 2021, **14**, 4534–4540.

64 J. Wan, Z. Zhao, H. Shang, B. Peng, W. Chen, J. Pei, L. Zheng, J. Dong, R. Cao, R. Sarangi, Z. Jiang, D. Zhou, Z. Zhuang, J. Zhang, D. Wang and Y. Li, *J. Am. Chem. Soc.*, 2020, **142**, 8431–8439.

5788 | *J. Mater. Chem. A*, 2022, **10**, 5771–5791

This journal is © The Royal Society of Chemistry 2022

65 A. Beheshti Askari, M. al Samarai, N. Hiraoka, H. Ishii, L. Tillmann, M. Muhler and S. DeBeer, *Nanoscale*, 2020, **12**, 15185–15192.

66 V. Pramhaas, M. Roiaz, N. Bosio, M. Corva, C. Rameshan, E. Vesselli, H. Grönbeck and G. Rupprechter, *ACS Catal.*, 2021, **11**, 208–214.

67 N. J. Divins, I. Angurell, C. Escudero, V. Pérez-Dieste and J. Llorca, *Science*, 2014, **346**, 620.

68 S. Zhu, X. Li, X. Jiao, W. Shao, L. Li, X. Zu, J. Hu, J. Zhu, W. Yan, C. Wang, Y. Sun and Y. Xie, *Nano Lett.*, 2021, **21**, 2324–2331.

69 S. Béchu, M. Ralaiarisoa, A. Etcheberry and P. Schulz, *Adv. Energy Mater.*, 2020, **10**, 1904007.

70 Y. Shi, Z. R. Ma, Y. Y. Xiao, Y. C. Yin, W. M. Huang, Z. C. Huang, Y. Z. Zheng, F. Y. Mu, R. Huang, G. Y. Shi, Y. Y. Sun, X. H. Xia and W. Chen, *Nat. Commun.*, 2021, **12**, 3021.

71 J. Ma, C. Gao, J. Low, D. Liu, X. Lian, H. Zhang, H. Jin, X. Zheng, C. Wang, R. Long, H. Ji, J. Zhu and Y. Xiong, *J. Phys. Chem. C*, 2021, **125**, 5542–5548.

72 J. Xu, Z. Ju, W. Zhang, Y. Pan, J. Zhu, J. Mao, X. Zheng, H. Fu, M. Yuan, H. Chen and R. Li, *Angew. Chem., Int. Ed.*, 2021, **133**, 8787–8791.

73 C. Lv, L. Zhong, H. Liu, Z. Fang, C. Yan, M. Chen, Y. Kong, C. Lee, D. Liu, S. Li, J. Liu, L. Song, G. Chen, Q. Yan and G. Yu, *Nature Sustain.*, 2021, **4**, 868–876.

74 C. Hu, X. Wang, Z. Qi and C. Li, *Infrared Phys. Technol.*, 2020, **105**, 103200.

75 F. de Groot, *Chem. Rev.*, 2001, **101**, 1779–1808.

76 M. Wang, L. Árnadóttir, Z. J. Xu and Z. Feng, *Nano-Micro Lett.*, 2019, **11**, 47.

77 W. Qu, X. Liu, J. Chen, Y. Dong, X. Tang and Y. Chen, *Nat. Commun.*, 2020, **11**, 1532.

78 G. Wang, C.-T. He, R. Huang, J. Mao, D. Wang and Y. Li, *J. Am. Chem. Soc.*, 2020, **142**, 19339–19345.

79 L. Jiao, R. Zhang, G. Wan, W. Yang, X. Wan, H. Zhou, J. Shui, S. H. Yu and H. L. Jiang, *Nat. Commun.*, 2020, **11**, 2831.

80 J. J. Rehr, J. J. Kas, F. D. Vila, M. P. Prange and K. Jorissen, *Phys. Chem. Chem. Phys.*, 2010, **12**, 5503–5513.

81 Y. Chen, R. Gao, S. Ji, H. Li, K. Tang, P. Jiang, H. Hu, Z. Zhang, H. Hao, Q. Qu, X. Liang, W. Chen, J. Dong, D. Wang and Y. Li, *Angew. Chem., Int. Ed.*, 2021, **60**, 3212–3221.

82 P. Fornasini and R. Grisenti, *J. Synchrotron Radiat.*, 2015, **22**, 1242–1257.

83 Z. Yang, Y. Wang, M. Zhu, Z. Li, W. Chen, W. Wei, T. Yuan, Y. Qu, Q. Xu, C. Zhao, X. Wang, P. Li, Y. Li, Y. Wu and Y. Li, *ACS Catal.*, 2019, **9**, 2158–2163.

84 H. Zhang, W. Zhou, T. Chen, B. Y. Guan, Z. Li and X. W. Lou, *Energy Environ. Sci.*, 2018, **11**, 1980–1984.

85 H. Su, W. Zhou, W. Zhou, Y. Li, L. Zheng, H. Zhang, M. Liu, X. Zhang, X. Sun, Y. Xu, F. Hu, J. Zhang, T. Hu, Q. Liu and S. Wei, *Nat. Commun.*, 2021, **12**, 6118.

86 H. Gu, X. Liu, X. Liu, C. Ling, K. Wei, G. Zhan, Y. Guo and L. Zhang, *Nat. Commun.*, 2021, **12**, 5422.

87 D. Cao, D. Liu, S. Chen, O. A. Moses, X. Chen, W. Xu, C. Wu, L. Zheng, S. Chu, H. Jiang, C. Wang, B. Ge, X. Wu, J. Zhang and L. Song, *Energy Environ. Sci.*, 2021, **14**, 906–915.

88 S. C. Lin, C. C. Chang, S. Y. Chiu, H. T. Pai, T. Y. Liao, C. S. Hsu, W. H. Chiang, M. K. Tsai and H. M. Chen, *Nat. Commun.*, 2020, **11**, 3525.

89 C. Genovese, M. E. Schuster, E. K. Gibson, D. Gianolio, V. Posligua, R. Grau Crespo, G. Cibin, P. P. Wells, D. Garai, V. Solokha, S. Krick Calderon, J. J. Velasco Velez, C. Ampelli, S. Perathoner, G. Held, G. Centi and R. Arrigo, *Nat. Commun.*, 2018, **9**, 935.

90 F. Wang, J. Ma, S. Xin, Q. Wang, J. Xu, C. Zhang, H. He and X. Cheng Zeng, *Nat. Commun.*, 2020, **11**, 529.

91 Q. He, D. Liu, J. H. Lee, Y. Liu, Z. Xie, S. Hwang, S. Kattel, L. Song and J. G. Chen, *Angew. Chem., Int. Ed.*, 2020, **59**, 3033–3037.

92 J. Shan, C. Ye, S. Chen, T. Sun, Y. Jiao, L. Liu, C. Zhu, L. Song, Y. Han, M. Jaroniec, Y. Zhu, Y. Zheng and S. Z. Qiao, *J. Am. Chem. Soc.*, 2021, **143**, 5201–5211.

93 H. Kim, D. Shin, W. Yang, D. H. Won, H. S. Oh, M. W. Chung, D. Jeong, S. H. Kim, K. H. Chae, J. Y. Ryu, J. Lee, S. J. Cho, J. Seo, H. Kim and C. H. Choi, *J. Am. Chem. Soc.*, 2021, **143**, 925–933.

94 M. Bajdich, M. García-Mota, A. Vojvodic, J. K. Nørskov and A. T. Bell, *J. Am. Chem. Soc.*, 2013, **135**, 13521–13530.

95 F. Maurer, J. Jelic, J. Wang, A. Gänzler, P. Dolcet, C. Wöll, Y. Wang, F. Studt, M. Casapu and J. D. Grunwaldt, *Nat. Catal.*, 2020, **3**, 824–833.

96 A. de Juan, J. Jaumot and R. Tauler, *Anal. Methods*, 2014, **6**, 4964–4976.

97 J. Jaumot, A. de Juan and R. Tauler, *Chemom. Intell. Lab. Syst.*, 2015, **140**, 1–12.

98 A. L. Ankudinov, J. J. Rehr, J. J. Low and S. R. Bare, *J. Chem. Phys.*, 2002, **116**, 1911–1919.

99 O. Bunău and Y. Joly, *J. Phys.: Condens. Matter*, 2009, **21**, 345501.

100 M. Xiao, J. Zhu, S. Li, G. Li, W. Liu, Y. P. Deng, Z. Bai, L. Ma, M. Feng, T. Wu, D. Su, J. Lu, A. Yu and Z. Chen, *ACS Catal.*, 2021, **11**, 8837–8846.

101 D. Liu, Q. He, S. Ding and L. Song, *Adv. Energy Mater.*, 2020, **10**, 2001482.

102 S. Li, M. Dong, J. Yang, X. Cheng, X. Shen, S. Liu, Z. Q. Wang, X. Q. Gong, H. Liu and B. Han, *Nat. Commun.*, 2021, **12**, 584.

103 J. Feng, H. Gao, L. Zheng, Z. Chen, S. Zeng, C. Jiang, H. Dong, L. Liu, S. Zhang and X. Zhang, *Nat. Commun.*, 2020, **11**, 4341.

104 M. Zhou, Y. Jiang, G. Wang, W. Wu, W. Chen, P. Yu, Y. Lin, J. Mao and L. Mao, *Nat. Commun.*, 2020, **11**, 3188.

105 Y. Zhou, X. Tao, G. Chen, R. Lu, D. Wang, M.-X. Chen, E. Jin, J. Yang, H.-W. Liang, Y. Zhao, X. Feng, A. Narita and K. Müllen, *Nat. Commun.*, 2020, **11**, 5892.

106 S. Feng, X. Song, Y. Liu, X. Lin, L. Yan, S. Liu, W. Dong, X. Yang, Z. Jiang and Y. Ding, *Nat. Commun.*, 2019, **10**, 5281.

107 J. Liu, C. Cao, X. Liu, L. Zheng, X. Yu, Q. Zhang, L. Gu, R. Qi and W. Song, *Angew. Chem., Int. Ed.*, 2021, **60**, 15248–15253.

This journal is © The Royal Society of Chemistry 2022

J. Mater. Chem. A, 2022, **10**, 5771–5791 | **5789**

108 H. Jing, Z. Zhao, C. Zhang, W. Liu, D. Wu, C. Zhu, C. Hao, J. Zhang and Y. Shi, *Nano Res.*, 2021, **14**, 4025–4032.

109 A. Kumar, X. Liu, J. Lee, B. Debnath, A. R. Jadhav, X. Shao, V. Q. Bui, Y. Hwang, Y. Liu, M. G. Kim and H. Lee, *Energy Environ. Sci.*, 2021, DOI: 10.1039/d1ee02603h.

110 X. Chen, J. Wan, J. Wang, Q. Zhang, L. Gu, L. Zheng, N. Wang and R. Yu, *Adv. Mater.*, 2021, 2104764.

111 C. Tang, Y. Jiao, B. Shi, J. N. Liu, Z. Xie, X. Chen, Q. Zhang and S. Z. Qiao, *Angew. Chem., Int. Ed.*, 2020, **59**, 9171–9176.

112 K. Liu, X. Zhao, G. Ren, T. Yang, Y. Ren, A. F. Lee, Y. Su, X. Pan, J. Zhang, Z. Chen, J. Yang, X. Liu, T. Zhou, W. Xi, J. Luo, C. Zeng, H. Matsumoto, W. Liu, Q. Jiang, K. Wilson, A. Wang, B. Qiao, W. Li and T. Zhang, *Nat. Commun.*, 2020, **11**, 1263.

113 H. Xu, D. Rebollar, H. He, L. Chong, Y. Liu, C. Liu, C. J. Sun, T. Li, J. V. Muntean, R. E. Winans, D. J. Liu and T. Xu, *Nat. Energy*, 2020, **5**, 623–632.

114 H. Shang, T. Wang, J. Pei, Z. Jiang, D. Zhou, Y. Wang, H. Li, J. Dong, Z. Zhuang, W. Chen, D. Wang, J. Zhang and Y. Li, *Angew. Chem., Int. Ed.*, 2020, **59**, 22465–22469.

115 J. Xu, X. Zheng, Z. Feng, Z. Lu, Z. Zhang, W. Huang, Y. Li, D. Vuckovic, Y. Li, S. Dai, G. Chen, K. Wang, H. Wang, J. K. Chen, W. Mitch and Y. Cui, *Nat. Sustain.*, 2021, **4**, 233–241.

116 X. Li, Y. Zeng, C. W. Tung, Y. R. Lu, S. Baskaran, S. F. Hung, S. Wang, C. Q. Xu, J. Wang, T. S. Chan, H. M. Chen, J. Jiang, Q. Yu, Y. Huang, J. Li, T. Zhang and B. Liu, *ACS Catal.*, 2021, **11**, 7292–7301.

117 L. Cao, Q. Luo, W. Liu, Y. Lin, X. Liu, Y. Cao, W. Zhang, Y. Wu, J. Yang, T. Yao and S. Wei, *Nat. Catal.*, 2019, **2**, 134–141.

118 Y. Pan, Y. Chen, K. Wu, Z. Chen, S. Liu, X. Cao, W.-C. Cheong, T. Meng, J. Luo, L. Zheng, C. Liu, D. Wang, Q. Peng, J. Li and C. Chen, *Nat. Commun.*, 2019, **10**, 4290.

119 N. Zhang, T. Zhou, M. Chen, H. Feng, R. Yuan, C. a. Zhong, W. Yan, Y. Tian, X. Wu, W. Chu, C. Wu and Y. Xie, *Energy Environ. Sci.*, 2020, **13**, 111–118.

120 L. Han, M. Hou, P. Ou, H. Cheng, Z. Ren, Z. Liang, J. A. Boscoboinik, A. Hunt, I. Waluyo, S. Zhang, L. Zhuo, J. Song, X. Liu, J. Luo and H. L. Xin, *ACS Catal.*, 2021, **11**, 509–516.

121 J. Zhou, L. Zhang, Y. C. Huang, C. L. Dong, H. J. Lin, C. T. Chen, L. H. Tjeng and Z. Hu, *Nat. Commun.*, 2020, **11**, 1984.

122 X. Zheng, B. Zhang, P. De Luna, Y. Liang, R. Comin, O. Voznyy, L. Han, F. P. García de Arquer, M. Liu, C. T. Dinh, T. Regier, J. J. Dynes, S. He, H. L. Xin, H. Peng, D. Prendergast, X. Du and E. H. Sargent, *Nat. Chem.*, 2018, **10**, 149–154.

123 J. Li and J. Gong, *Energy Environ. Sci.*, 2020, **13**, 3748–3779.

124 S. Y. Chang, A. Uehara, S. G. Booth, K. Ignatyev, J. F. W. Mosselmans, R. A. W. Dryfe and S. L. M. Schroeder, *RSC Adv.*, 2015, **5**, 6912–6918.

125 S. Fang, X. Zhu, X. Liu, J. Gu, W. Liu, D. Wang, W. Zhang, Y. Lin, J. Lu, S. Wei, Y. Li and T. Yao, *Nat. Commun.*, 2020, **11**, 1029.

126 X. Li, S. Wang, L. Li, Y. Sun and Y. Xie, *J. Am. Chem. Soc.*, 2020, **142**, 9567–9581.

127 J. Cored, A. García-Ortiz, S. Iborra, M. J. Climent, L. Liu, C. H. Chuang, T. S. Chan, C. Escudero, P. Concepción and A. Corma, *J. Am. Chem. Soc.*, 2019, **141**, 19304–19311.

128 L. Han, L. Zhang, H. Wu, H. Zu, P. Cui, J. Guo, R. Guo, J. Ye, J. Zhu, X. Zheng, L. Yang, Y. Zhong, S. Liang and L. Wang, *Adv. Sci.*, 2019, **6**, 1900006.

129 X. Zu, Y. Zhao, X. Li, R. Chen, W. Shao, Z. Wang, J. Hu, J. Zhu, Y. Pan, Y. Sun and Y. Xie, *Angew. Chem., Int. Ed.*, 2021, **133**, 13959–13965.

130 L. Cao, W. Liu, Q. Luo, R. Yin, B. Wang, J. Weissenrieder, M. Soldemo, H. Yan, Y. Lin, Z. Sun, C. Ma, W. Zhang, S. Chen, H. Wang, Q. Guan, T. Yao, S. Wei, J. Yang and J. Lu, *Nature*, 2019, **565**, 631–635.

131 L. Nguyen, F. F. Tao, Y. Tang, J. Dou and X. J. Bao, *Chem. Rev.*, 2019, **119**, 6822–6905.

132 M. G. Sibi, D. Verma, H. C. Setiyadi, M. K. Khan, N. Karanwal, S. K. Kwak, K. Y. Chung, J. H. Park, D. Han, K. W. Nam and J. Kim, *ACS Catal.*, 2021, **11**, 8382–8398.

133 K. Roy, L. Artiglia and J. A. van Bokhoven, *ChemCatChem*, 2018, **10**, 666–682.

134 D. Cao, O. A. Moses, B. Sheng, S. Chen, H. Pan, L. Wu, H. Shou, W. Xu, D. Li, L. Zheng, S. Chu, C. Hu, D. Liu, S. Wei, X. Zheng, Z. Qi, X. Wu, J. Zhang and L. Song, *Sci. Bull.*, 2021, **66**, 553–561.

135 S. Liu, H. B. Yang, S. F. Hung, J. Ding, W. Cai, L. Liu, J. Gao, X. Li, X. Ren, Z. Kuang, Y. Huang, T. Zhang and B. Liu, *Angew. Chem., Int. Ed.*, 2020, **59**, 798–803.

136 A. C. Schilling, K. Groden, J. P. Simonovis, A. Hunt, R. T. Hannagan, V. Çınar, J. S. McEwen, E. C. H. Sykes and I. Waluyo, *ACS Catal.*, 2020, **10**, 4215–4226.

137 S. Wu, K. Y. Tseng, R. Kato, T. S. Wu, A. Large, Y. K. Peng, W. Xiang, H. Fang, J. Mo, I. Wilkinson, Y. L. Soo, G. Held, K. Suenaga, T. Li, H. Y. T. Chen and S. C. E. Tsang, *J. Am. Chem. Soc.*, 2021, **143**, 9105–9112.

138 V. Muravev, G. Spezzati, Y. Q. Su, A. Parastaev, F. K. Chiang, A. Longo, C. Escudero, N. Kosinov and E. J. M. Hensen, *Nat. Catal.*, 2021, **4**, 469–478.

139 G. N. Vayssilov, Y. Lykhach, A. Migani, T. Staudt, G. P. Petrova, N. Tsud, T. Skála, A. Bruix, F. Illas, K. C. Prince, V. r. Matolín, K. M. Neyman and J. Libuda, *Nat. Mater.*, 2011, **10**, 310–315.

140 A. Neitzel, A. Figueroba, Y. Lykhach, T. Skála, M. Vorokhta, N. Tsud, S. Mehl, K. Ševčíková, K. C. Prince, K. M. Neyman, V. Matolín and J. Libuda, *J. Phys. Chem. C*, 2016, **120**, 9852–9862.

141 Y. Ma, Y. Ren, Y. Zhou, W. Liu, W. Baaziz, O. Ersen, C. Pham Huu, M. Greiner, W. Chu, A. Wang, T. Zhang and Y. Liu, *Angew. Chem., Int. Ed.*, 2020, **59**, 21613–21619.

142 F. Tao, S. Dag, L. W. Wang, Z. Liu, D. R. Butcher, H. Bluhm, M. Salmeron and G. A. Somorjai, *Science*, 2010, **327**, 850.

143 J. Yang, W. Li, D. Wang and Y. Li, *Adv. Mater.*, 2020, **32**, 2003300.

144 X. Li, Y. Sun, J. Xu, Y. Shao, J. Wu, X. Xu, Y. Pan, H. Ju, J. Zhu and Y. Xie, *Nat. Energy*, 2019, **4**, 690–699.

5790 | *J. Mater. Chem. A*, 2022, **10**, 5771–5791

This journal is © The Royal Society of Chemistry 2022

145 M. Xiao, L. Gao, Y. Wang, X. Wang, J. Zhu, Z. Jin, C. Liu, H. Chen, G. Li, J. Ge, Q. He, Z. Wu, Z. Chen and W. Xing, *J. Am. Chem. Soc.*, 2019, **141**, 19800–19806.

146 C. Gao, S. Chen, Y. Wang, J. Wang, X. Zheng, J. Zhu, L. Song, W. Zhang and Y. Xiong, *Adv. Mater.*, 2018, **30**, 1704624.

147 C. Gao, Q. Meng, K. Zhao, H. Yin, D. Wang, J. Guo, S. Zhao, L. Chang, M. He, Q. Li, H. Zhao, X. Huang, Y. Gao and Z. Tang, *Adv. Mater.*, 2016, **28**, 6485–6490.

148 Z. Wang, J. Yang, J. Gan, W. Chen, F. Zhou, X. Zhou, Z. Yu, J. Zhu, X. Duan and Y. Wu, *J. Mater. Chem. A*, 2020, **8**, 10755–10760.

149 F. Tao, M. E. Grass, Y. Zhang, D. R. Butcher, J. R. Renzas, Z. Liu, J. Y. Chung, B. S. Mun, M. Salmeron and G. A. Somorjai, *Science*, 2008, **322**, 932.

150 S. Li, J. Liu, Z. Yin, P. Ren, L. Lin, Y. Gong, C. Yang, X. Zheng, R. Cao, S. Yao, Y. Deng, X. Liu, L. Gu, W. Zhou, J. Zhu, X. Wen, B. Xu and D. Ma, *ACS Catal.*, 2020, **10**, 907–913.

151 Y. Lu, J. Wang, L. Yu, L. Kovarik, X. Zhang, A. S. Hoffman, A. Gallo, S. R. Bare, D. Sokaras, T. Kroll, V. Dagle, H. Xin and A. M. Karim, *Nat. Catal.*, 2019, **2**, 149–156.

152 W. Duncan and G. Williams, *Appl. Opt.*, 1983, **22**, 2914–2923.

153 F. N. Ajjan, M. J. Jafari, T. Rębiś, T. Ederth and O. Inganäs, *J. Mater. Chem. A*, 2015, **3**, 12927–12937.

154 X. Tao, R. Long, D. Wu, Y. Hu, G. Qiu, Z. Qi, B. Li, R. Jiang and Y. Xiong, *Small*, 2020, **16**, 2001782.

155 C. Wu, S. Ding, D. Liu, D. Li, S. Chen, H. Wang, Z. Qi, B. Ge and L. Song, *Research*, 2020, **2020**, 5860712.

156 W. Zhou, H. Su, Z. Wang, F. Yu, W. Wang, X. Chen and Q. Liu, *J. Mater. Chem. A*, 2021, **9**, 1127–1133.

157 H. Shang, X. Zhou, J. Dong, A. Li, X. Zhao, Q. Liu, Y. Lin, J. Pei, Z. Li, Z. Jiang, D. Zhou, L. Zheng, Y. Wang, J. Zhou, Z. Yang, R. Cao, R. Sarangi, T. Sun, X. Yang, X. Zheng, W. Yan, Z. Zhuang, J. Li, W. Chen, D. Wang, J. Zhang and Y. Li, *Nat. Commun.*, 2020, **11**, 3049.

158 H. Su, W. Zhou, H. Zhang, W. Zhou, X. Zhao, Y. Li, M. Liu, W. Cheng and Q. Liu, *J. Am. Chem. Soc.*, 2020, **142**, 12306–12313.

159 W. Ye, S. Chen, Y. Lin, L. Yang, S. Chen, X. Zheng, Z. Qi, C. Wang, R. Long, M. Chen, J. Zhu, P. Gao, L. Song, J. Jiang and Y. Xiong, *Chem*, 2019, **5**, 2865–2878.

160 D. Cao, H. Shou, S. Chen and L. Song, *Curr. Opin. Electrochem.*, 2021, **30**, 100788.

161 S. G. Han, D. D. Ma and Q. L. Zhu, *Small Methods*, 2021, **5**, 2100102.

162 I. Lezcano-González, R. Oord, M. Rovezzi, P. Glatzel, S. W. Botchway, B. M. Weckhuysen and A. M. J. A. C. Beale, *Angew. Chem., Int. Ed.*, 2016, **128**, 5301–5305.

163 C. Liu, J. Qian, Y. Ye, H. Zhou, C. J. Sun, C. Sheehan, Z. Zhang, G. Wan, Y.-S. Liu, J. Guo, S. Li, H. Shin, S. Hwang, T. B. Gunnoe, W. A. Goddard and S. Zhang, *Nat. Catal.*, 2021, **4**, 36–45.

164 Y. Dai, T. J. Gorey, S. L. Anderson, S. Lee, S. Lee, S. Seifert and R. E. Winans, *J. Phys. Chem. C*, 2017, **121**, 361.

165 J. Timoshenko, A. Halder, B. Yang, S. Seifert, M. J. Pellin, S. Vajda and A. I. Frenkel, *J. Phys. Chem. C*, 2018, **122**, 21686.

166 L. Fang, S. Seifert, R. E. Winans and T. Li, *Small Methods*, 2021, **5**, 2001194.

167 B. Chen, X. Zhong, G. Zhou, N. Zhao and H. M. Cheng, *Adv. Mater.*, 2021, 2105812.

168 X. Wang, Y. Li, Y. Wang, H. Zhang, Z. Jin, X. Yang, Z. Shi, L. Liang, Z. Wu, Z. Jiang, W. Zhang, C. Liu, W. Xing and J. Ge, *Proc. Natl. Acad. Sci. U. S. A.*, 2021, **118**, e2107332118.

169 X. Cheng, J. Yang, W. Yan, Y. Han, X. Qu, S. Yin, C. Chen, R. Ji, Y. Li, G. Li, G. Li, Y. Jiang and S. Sun, *Energy Environ. Sci.*, 2021, **14**, 5958–5967.

170 Y. Yan, S. Liang, X. Wang, M. Zhang, S.-M. Hao, X. Cui, Z. Li and Z. Lin, *Proc. Natl. Acad. Sci. U. S. A.*, 2021, **118**, e2110036118.

171 B. W. Zhang, T. Sheng, Y. D. Liu, Y. X. Wang, L. Zhang, W. H. Lai, L. Wang, J. Yang, Q. F. Gu, S. L. Chou, H. K. Liu and S. X. Dou, *Nat. Commun.*, 2018, **9**, 4082.

This journal is © The Royal Society of Chemistry 2022

J. Mater. Chem. A, 2022, **10**, 5771–5791 | 5791